Theory of double-resonant Raman spectra in graphene: Intensity and line shape of defect-induced and two-phonon bands

Pedro Venezuela,[1,2] Michele Lazzeri,[1] and Francesco Mauri[1]
[1]*IMPMC, Université Pierre et Marie Curie, CNRS, 4 place Jussieu, F-75252 Paris, France*
[2]*Instituto de Física, Universidade Federal Fluminense, 24210-346 Niterói, RJ, Brazil*
(Received 23 March 2011; published 25 July 2011)

We calculate the double-resonant (DR) Raman spectrum of graphene, and determine the lines associated to both phonon-defect processes (such as in the D line at $\sim$1350 cm^{-1}, D' at $\sim$1600 cm^{-1}, and D'' at $\sim$1100 cm^{-1}), and two-phonon ones (such as in the $2D$, $2D'$, or $D+D''$ lines). Phonon and electronic dispersions reproduce calculations based on density-functional theory corrected with GW. Electron-light, -phonon, and -defect scattering matrix elements and the electronic linewidth are explicitly calculated. Defect-induced processes are simulated by considering different kinds of idealized defects. For an excitation energy of $\epsilon_L = 2.4$ eV, the agreement with measurements is very good and calculations reproduce the relative intensities among phonon-defect or among two-phonon lines; the measured small widths of the D, D', $2D$, and $2D'$ lines; the line shapes; the presence of small intensity lines in the 1800–2000-cm^{-1} range. We determine how the spectra depend on the excitation energy, on the light polarization, on the electronic linewidth, on the kind of defects, and on their concentration. According to the present findings, the intensity ratio between the $2D'$ and $2D$ lines can be used to determine experimentally the electronic linewidth. The intensity ratio between the D and D' lines depends on the kind of model defect, suggesting that this ratio could possibly be used to identify the kind of defects present in actual samples. Charged impurities outside the graphene plane provide an almost undetectable contribution to the Raman signal. The present analysis reveals that, for both D and $2D$ lines, the dominant DR processes are those in which electrons and holes are both involved in the scattering, because of a destructive quantum interference that kills processes involving only electrons or only holes. The most important phonons belong to the $\mathbf{K} \rightarrow \mathbf{\Gamma}$ direction (*inner* phonons) and not to the $\mathbf{K} \rightarrow \mathbf{M}$ one (*outer* phonons), as usually assumed. The small $2D$ linewidth at $\epsilon_L = 2.4$ eV is a consequence of the interplay between the opposite trigonal warpings of the electron and phonon dispersions. At higher excitation, e.g., $\epsilon_L = 3.8$ eV, the $2D$ line becomes broader and evolves in an asymmetric double peak structure.

DOI: 10.1103/PhysRevB.84.035433 PACS number(s): 78.30.−j, 78.67.Wj, 81.05.ue

I. INTRODUCTION

Raman spectroscopy is one of the most important experimental techniques for the characterization of graphitic materials. In particular, for graphene, this technique provides information about the number of layers,[1,2] doping,[3–5] disorder,[6–8] and phonon properties .[9]

Lowest-oder Raman processes correspond to the scattering with a zero-momentum phonon ($\mathbf{q} = \mathbf{0}$). The Raman G line in graphene and graphite ($\sim$1582 cm^{-1}) is associated with the E_{2g} phonon at $\mathbf{\Gamma}$ and it is a lowest-order process. Graphene and graphite present other lines, due to higher-order processes, which are usually interpreted in terms of the so-called double-resonance (DR) mechanism.[10] The DR mechanism is used to interpret two distinct kinds of phenomena. The first is the excitation of a phonon with momentum $\mathbf{q} \neq \mathbf{0}$ due to the presence of defects in the sample. This process, called *defect induced*, is not allowed in a purely crystalline sample (without defects) because of momentum conservation. In graphene and graphite, it gives rise to the well studied D line at $\sim$1350 cm^{-1} and also to less intense lines such as the D' ($\sim$1600 cm^{-1}) and the D'' [$\sim$1100 cm^{-1} (Refs. 7 and 11)]. The second process corresponds to the excitation of two phonons with opposite momenta $\mathbf{q}$ and $-\mathbf{q}$. This process, called *two phonon*, can be observed in purely crystalline samples since the momentum is conserved and gives rise to the very intense $2D$ line at $\sim$2700 cm^{-1} (which is an overtone of the D line) and, for instance, to the $D+D''$ and $2D'$ lines at $\sim$2450 cm^{-1} and $\sim$3200 cm^{-1}. The lines related to DR defect-induced and two-phonon processes have a remarkable property: they are dispersive, i.e., their positions change with excitation energy.

It has been shown experimentally[1,2] that the $2D$ line in graphene changes in shape, width, and position with the number of layers. Later, the phonon dispersion of graphene, near the Dirac $\mathbf{K}$ points, was probed by measurements[9] of the $2D$ and $D+D''$ lines as a function of the excitation energies. Usually, Raman experiments are performed in graphene layers that were deposited or grown over a substrate. However, experimental measurements of the G and $2D$ lines have also been performed for free-standing graphene monolayers.[12] Lucchese *et al.*[7] and Martins Ferreira *et al.*[11] have studied the evolution of the Raman spectra for mono- and multilayer graphene with increasing disorder, showing that the intensity of the D line, which is absent in pristine graphene, increases when disorder is induced in the sample up to a maximum value where it begins to decrease. On the other hand, the $2D$ line intensity is maximum for pristine graphene and it decreases with increasing disorder.

Frequencies, intensities, and linewidths of all DR Raman bands may be determined by the calculation of the Raman cross section.[13] Several excellent theoretical works already appeared on the topic providing an overall good understanding of the situation. However, the many different approximations used by different authors (e.g., constant electron-phonon matrix

elements, resonant phonons are assumed to be on some high-symmetry line, in some cases the electronic dispersion is conic, the electronic lifetime is a parameter, etc.) and the several debates still going on lead to the sensation that something is missing. Thomsen and Reich[10] and Kurti *et al.*[14] studied the D line for graphite and carbon nanotubes, respectively. Also, Narula and Reich[15] studied the D and $2D$ Raman lines in graphene and graphite. In these works[10,14,15] the scattering matrix elements (electron light, electron phonon, and electron defect) are assumed to be constants and the electronic linewidth is a parameter set to a fixed value. Basko[16] has studied the two-phonon and four-phonon Raman bands in graphene under the assumption of conical bands, which is valid only in the limit of small excitation energies, not suitable for most experimental data available in the literature. Also, his work is limited to disorder-free graphene. Park *et al.*[17] have studied the two-phonon processes in single, double, and triple layer graphene, making the assumption of conical bands and limiting their work to disorder-free graphene.

In this context, some questions are currently debated. For instance, according to previous theoretical works,[10,14,15] phonons in the $\mathbf{K} \rightarrow \mathbf{M}$ direction of the Brillouin zone should give the most important contribution to the D line intensity. However, recent works[18–22] have argued that the phonons in the $\mathbf{K} \rightarrow \mathbf{\Gamma}$ direction should be more important. Other open questions refer to the processes more relevant for the DR Raman spectra. In some Raman processes only the electrons are scattered, while in other processes both electrons and holes are scattered simultaneously. Some authors claim that, at least for the $2D$ line, this last kind of process should be dominant because they are associated to a triple resonance.[23] On the other hand, several authors perform their studies considering only electron-electron processes, as in the seminal work by Thomsen and Reich.[10]

Besides, several fundamental questions are almost untouched. So far, the DR mechanism has been basically used to give an overall description of the physics and to determine which are the excited phonons. Can the DR theory be used to obtain a quantitative description of the intensities of the Raman lines? Can the DR theory be used to obtain a quantitative description of the shape and of the width of the Raman lines? The most studied Raman lines, the $2D$ and the D ones, present a relatively narrow linewidth similar to the one of the G line (which is not due to DR). This fact is very surprising and, indeed, the theoretical approaches used so far were not able to reproduce the observed small width of these lines. Which are the missing ingredients? Is this a consequence of the approximations used so far, or, on the contrary, is this a limit of the perturbative approach inherent to the DR theory? Finally, the D line is activated by disorder and is routinely used to probe the quality of the samples of graphitic materials. However, which kind of defects activate the D line is not known. For instance, do neutral impurities, vacancies, and charged defects affect the D line in the same way? Which kind of defects are probed by measuring different defect-activates lines? Does Raman spectroscopy probe the defects, which mostly influence electronic transport?

Here, as a first step to answer these questions, we calculate the double-resonant Raman spectrum of graphene, considering both defect-induced and two-phonon processes, trying to provide a computational method overcoming the most common approximations used in literature. Calculations are done using the standard approach based on the golden rule generalized to the perturbative fourth order.[10] The electronic summation is performed all over the two-dimensional Brillouin zone and all the possible phonons (with any wave vector) are considered. The phonon dispersion is obtained from fully *ab initio* calculations based on density-functional theory (DFT) corrected with GW. Electronic structure calculations are based on a tight-binding approach in which the parameters are fitted to reproduce DFT + GW calculations. The electronic lifetime is calculated explicitly and the defect-induced processes are simulated by considering three different kinds of ideal model defects.

Section II describes the computational method; Sec. III describes and discusses the results; Sec. IV resumes the main conclusions of the paper.

II. METHOD

This section describes the method used to compute the DR Raman spectra. Section II A gives the general framework and provides the equations to obtain double-resonant Raman spectra in graphene within the perturbative approach. The other subsections describe the details to obtain the quantities used in the actual implementation. In particular, Sec. II B describes the electronic and phononic band dispersions; Secs. II C, II D, and II E describe the electron-phonon, electron-light, and electron-defect scattering matrix elements; Sec. II F describes the calculation of the electronic linewidth.

A. Double-resonant Raman intensity

In vibrational Raman, the spectrum usually consists in well defined lines associated with emission (Stokes) or absorption (anti-Stokes) of a phonon. Here, only Stokes processes are considered. Note also that the G line (lowest-order excitation of the E_{2g} $\mathbf{\Gamma}$ phonon) is not described by the present formalism and is thus not present in the calculated spectra. Within the DR scheme,[10] the light-electron and electron-phonon interactions, as well as the defect-induced electron-electron scattering, are treated at the first order in perturbation theory. The Raman cross section I of the light scattered by a crystal is obtained from the golden rule generalized to the fourth order:[13]

$$I \propto \sum_f \left| \sum_{A,B,C} \frac{\mathcal{M}_{fC}\mathcal{M}_{CB}\mathcal{M}_{BA}\mathcal{M}_{Ai}}{\left(\epsilon_i - \epsilon_C - i\frac{\gamma^C}{2}\right)\left(\epsilon_i - \epsilon_B - i\frac{\gamma^B}{2}\right)\left(\epsilon_i - \epsilon_A - i\frac{\gamma^A}{2}\right)} \right|^2 \delta(\epsilon_i - \epsilon_f), \quad (1)$$

where ϵ_i is the energy of the initial state, which consists of a quantum of light with energy $\epsilon_L = \hbar\omega_L$ (the laser energy) and in which the crystal is in the ground state. The sum is performed on intermediate virtual states A, B, C, with energy ϵ_A, ϵ_B, ϵ_C, which are described by electronic and phononic excitation of the crystal. ϵ_f is the energy of the final state f, in which the electronic degrees of freedom of the crystal are in the ground state, one or two phonons with total energy $\hbar\omega_p$ have been excited, and a quantum of light with energy $\epsilon_L - \hbar\omega_p$ has been emitted. δ is the Dirac distribution. γ^A, γ^B, γ^C are the inverse of the lifetimes of the electronic excitations of the virtual states A, B, C, respectively. $\mathcal{M}_{JK}$ are first-order scattering matrix elements between the states J and K. So far, no attempts have been reported to go beyond the approximation inherent to Eq. (1), for graphitic materials. Note that within the present approach, the G line (which in literature is usually referred to as a "first-order" process) is a third-order process.

The processes described by Eq. (1) are in general associated to lines which are much weaker than first-order Raman lines. Graphene and graphite are notable exceptions. During the intermediate virtual transition the energy is not necessarily conserved and the three denominators of Eq. (1) are in general different from zero. However, in graphene and graphite two or more of the denominators of Eq. (1) can be equal to zero simultaneously. In literature this is called a double-resonance condition, and can be associated to Raman lines that have an intensity comparable to that of lower-order processes (the G line).

In the DR Raman scattering, the process $\mathcal{M}_{Ai}$ in Eq. (1) corresponds to the absorption of light by creation of an electron-hole pair in the π/π^* bands. Then the carriers are scattered twice before recombination [$\mathcal{M}_{BA}$ and $\mathcal{M}_{CB}$ in Eq. (1)]. For temperatures typically present in Raman measurements in graphene, only Stoke processes (phonon emission) are relevant. Thus in one possible case, one scattering event is due to collision with a defect and the other to the creation of a phonon (*phonon-defect* process). In a second possible case, both scattering events are due to creation of phonons (*two-phonon* process). Finally, the process $\mathcal{M}_{fC}$ in Eq. (1) corresponds to the recombination of the carriers by light emission. We define $I^{pd}_{\mathbf{q}\nu}$ as the probability to excite a phonon $-\mathbf{q}\nu$, with momentum $-\mathbf{q}$, branch index ν, and energy $\hbar\omega^{\nu}_{-\mathbf{q}}$ through a *phonon-defect* process. $I^{pp}_{\mathbf{q}\nu\mu}$ is the probability to excite the two phonons $-\mathbf{q}\nu$ and $\mathbf{q}\mu$ through a *two-phonon* process. The Raman intensity as a function of the frequency ω of the scattered light is proportional to

$$\begin{aligned} I(\omega) = {} & \frac{1}{N_q}\sum_{\mathbf{q},\nu} I^{pd}_{\mathbf{q}\nu}\,\delta\left(\omega_L - \omega - \omega^{\nu}_{-\mathbf{q}}\right)\left[n(\omega^{\nu}_{-\mathbf{q}}) + 1\right] \\ & + \frac{1}{N_q}\sum_{\mathbf{q},\nu,\mu} I^{pp}_{\mathbf{q}\nu\mu}\,\delta\left(\omega_L - \omega - \omega^{\nu}_{-\mathbf{q}} - \omega^{\mu}_{\mathbf{q}}\right) \\ & \times \left[n\left(\omega^{\nu}_{-\mathbf{q}}\right) + 1\right]\left[n\left(\omega^{\mu}_{\mathbf{q}}\right) + 1\right], \end{aligned} \tag{2}$$

$$\begin{aligned} I^{pd}_{\mathbf{q}\nu} &= N_d \left| \frac{1}{N_k}\sum_{\mathbf{k},\alpha} K^{pd}_{\alpha}(\mathbf{k},\mathbf{q},\nu) \right|^2; \\ I^{pp}_{\mathbf{q}\nu\mu} &= \left| \frac{1}{N_k}\sum_{\mathbf{k},\beta} K^{pp}_{\beta}(\mathbf{k},\mathbf{q},\nu,\mu) \right|^2. \end{aligned} \tag{3}$$

The sum in Eq. (2) is performed on a uniform grid of N_q phonon wave vectors $\mathbf{q}$ in the Brillouin zone and on all the branch indexes ν and μ. In the limit $N_{\mathbf{q}} \to \infty$, $\delta(\omega)$ is the Dirac distribution. $n(\omega)$ is the Bose-Einstein occupation. In Eq. (3), N_d is the average number of defects in the unit cell. $I^{pd} \propto N_d$, because we assume that the contributions of defects on different sites add up incoherently. The first sum in Eq. (3) is performed on a uniform grid of N_k electronic wave vectors $\mathbf{k}$. α and β are labels running on the eight different possible processes that we call $ee1$,$ee2$,$hh1$,$hh2$,$eh1$,$eh2$,$he1$,$he2$, which are represented diagrammatically in Fig. 1. The reader might be familiar with an alternative representation of the processes, reported in Fig. 2. Expressions for the DR scattering amplitudes K are given in the appendixes. Here we report, as examples, K^{pd}_{ee1} and K^{pp}_{ee1}:

$$K^{pd}_{ee1}(\mathbf{k},\mathbf{q},\nu) = \frac{\langle \mathbf{k}\pi | D_{\text{out}} | \mathbf{k}\pi^* \rangle \langle \mathbf{k}\pi^* | H_D | \mathbf{k}+\mathbf{q},\pi^* \rangle \langle \mathbf{k}+\mathbf{q},\pi^* | \Delta H_{\mathbf{q},\nu} | \mathbf{k}\pi^* \rangle \langle \mathbf{k}\pi^* | D_{in} | \mathbf{k}\pi \rangle}{\left(\epsilon_L - \epsilon^{\pi^*}_{\mathbf{k}} + \epsilon^{\pi}_{\mathbf{k}} - \hbar\omega^{\nu}_{-\mathbf{q}} - i\frac{\gamma^C_{\mathbf{k}}}{2}\right)\left(\epsilon_L - \epsilon^{\pi^*}_{\mathbf{k}+\mathbf{q}} + \epsilon^{\pi}_{\mathbf{k}} - \hbar\omega^{\nu}_{-\mathbf{q}} - i\frac{\gamma^B_{\mathbf{k}}}{2}\right)\left(\epsilon_L - \epsilon^{\pi^*}_{\mathbf{k}} + \epsilon^{\pi}_{\mathbf{k}} - i\frac{\gamma^A_{\mathbf{k}}}{2}\right)}, \tag{4}$$

$$K^{pp}_{ee1}(\mathbf{k},\mathbf{q},\nu,\mu) = \frac{\langle \mathbf{k}\pi | D_{\text{out}} | \mathbf{k}\pi^* \rangle \langle \mathbf{k}\pi^* | \Delta H_{-\mathbf{q},\mu} | \mathbf{k}+\mathbf{q},\pi^* \rangle \langle \mathbf{k}+\mathbf{q},\pi^* | \Delta H_{\mathbf{q},\nu} | \mathbf{k}\pi^* \rangle \langle \mathbf{k}\pi^* | D_{in} | \mathbf{k}\pi \rangle}{\left(\epsilon_L - \epsilon^{\pi^*}_{\mathbf{k}} + \epsilon^{\pi}_{\mathbf{k}} - \hbar\omega^{\nu}_{-\mathbf{q}} - \hbar\omega^{\mu}_{\mathbf{q}} - i\frac{\gamma^C_{\mathbf{k}}}{2}\right)\left(\epsilon_L - \epsilon^{\pi^*}_{\mathbf{k}+\mathbf{q}} + \epsilon^{\pi}_{\mathbf{k}} - \hbar\omega^{\nu}_{-\mathbf{q}} - i\frac{\gamma^B_{\mathbf{k}}}{2}\right)\left(\epsilon_L - \epsilon^{\pi^*}_{\mathbf{k}} + \epsilon^{\pi}_{\mathbf{k}} - i\frac{\gamma^A_{\mathbf{k}}}{2}\right)}. \tag{5}$$

Equation (4) corresponds to the phonon-defect diagram $ee1$ in Fig. 1. Initially, the excitation laser creates an electron-hole pair with momentum $\mathbf{k}$. Thus using the notation of Eq. (1), $\mathcal{M}_{Ai} = \langle \pi^*\mathbf{k} | D_{in} | \pi\mathbf{k} \rangle$, where $|\mathbf{k}\pi\rangle$ and $|\mathbf{k}\pi^*\rangle$ are the electronic occupied and empty states and D_{in} is the operator coupling the incident electromagnetic wave with the crystal. $\epsilon_i = \epsilon_L$ and $\epsilon_A = \epsilon^{\pi^*}_{\mathbf{k}} - \varepsilon^{\pi}_{\mathbf{k}}$, with $\epsilon^{\pi}_{\mathbf{k}}$ the energy of $|\mathbf{k}\pi\rangle$. Second, the excited electron is scattered into a $\mathbf{k}+\mathbf{q}$ state by emitting a phonon with momentum $-\mathbf{q}$. Thus $\mathcal{M}_{BA} = \langle \mathbf{k}+\mathbf{q},\pi^* | \Delta H_{\mathbf{q},\nu} | \mathbf{k}\pi^* \rangle$, with $\Delta H_{\mathbf{q},\nu}$ the electron-phonon coupling operator. Now, $\varepsilon_B = \epsilon^{\pi^*}_{\mathbf{k}+\mathbf{q}} - \epsilon^{\pi}_{\mathbf{k}} + \hbar\omega^{\nu}_{-\mathbf{q}}$. The third step in the process K^{pd}_{ee1} is the scattering of the $\mathbf{k}+\mathbf{q}$ electron by a defect back to the $\mathbf{k}$ state. Thus $\mathcal{M}_{CB} = \langle \mathbf{k}\pi^* | H_D | \mathbf{k}+\mathbf{q},\pi^* \rangle$, with H_D the defect scattering operator and $\epsilon_C = \epsilon^{\pi^*}_{\mathbf{k}} - \epsilon^{\pi}_{\mathbf{k}} + \hbar\omega^{\nu}_{-\mathbf{q}}$. Finally, the electron and hole recombine vertically in the $\mathbf{k}$ state, by emitting light. Thus $\mathcal{M}_{fC} = \langle \mathbf{k}\pi | D_{\text{out}} | \mathbf{k}\pi^* \rangle$, with D_{out} the operator coupling the emitted photon with the crystal. The broadening energies $\gamma_{\mathbf{k}}$ in the denominators of the DR amplitudes K [e.g., in Eqs. (4) and (5)] are the inverse of the corresponding electronic lifetimes (see Sec. II F).

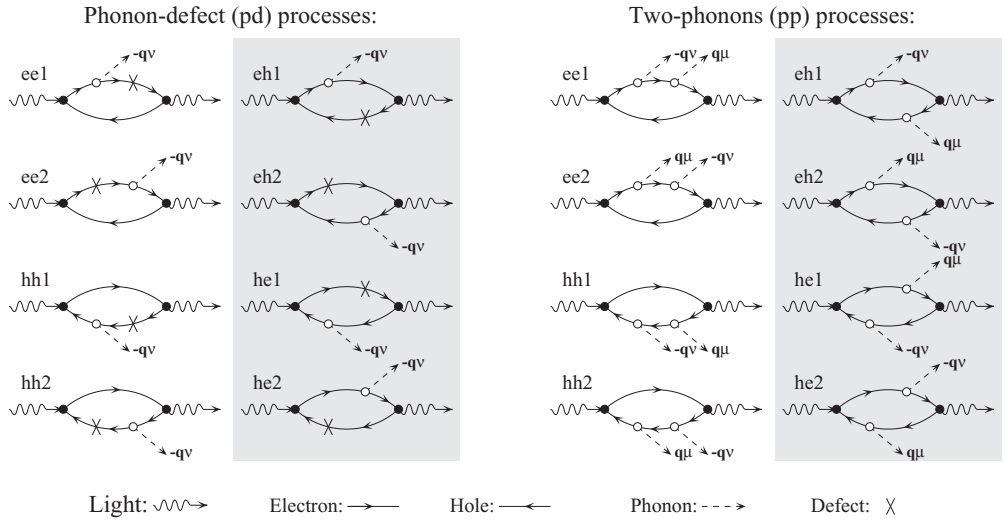

FIG. 1. Goldstone diagrams for the double-resonant Raman processes considered in this work. In this paper, the term "*ab* processes" refers to the processes highlighted by the gray area (*eh*1, *eh*2, *he*1, and *he*2). The other processes are referred to as "*aa* processes." The largest part of the Raman intensity is due to the *ab* processes. The reader might be familiar with an alternative representation of the processes, reported in Fig. 2.

Equation (5) corresponds to the phonon-phonon diagram *ee*1 in Fig. 1. The first two steps are the same as in the previous paragraph, while in the third step, the $\mathbf{k}+\mathbf{q}$ electron is scattered into a $\mathbf{k}$ electron, by emitting the phonon with momentum $\mathbf{q}\mu$. Thus $\mathcal{M}_{CB} = \langle \mathbf{k}\pi^* | \Delta H_{-\mathbf{q},\mu} | \mathbf{k}+\mathbf{q}\pi^* \rangle$ and $\epsilon_C = \epsilon^{\pi^*}_{\mathbf{k}} - \epsilon^{\pi}_{\mathbf{k}} + \hbar\omega^{\nu}_{-\mathbf{q}} + \hbar\omega^{\mu}_{\mathbf{q}}$. The fourth step is the same as before. Finally, for graphene and graphite, the diagrams of Fig. 1 are sometimes schematized with a different notation. For a comparison, see Fig. 2.

The sums in Eq. (2) are performed on a uniform grid of 120×120 $\mathbf{q}$ points (randomly shifted with respect to the origin) and $\delta(\omega)$ is a Lorentzian distribution with 8 cm^{-1} full width at half maximum. The results will be plotted as a function of the Raman shift $\omega_L - \omega$. The sums in Eq. (3) are performed on grids of $\mathbf{k}$ points that are sufficiently large to ensure convergence. Depending on the value of $\gamma^0_{\mathbf{k}}$, uniform grids between 480×480 and 840×840 $\mathbf{k}$ points are used. In Eq. (2), we consider $\hbar\omega^{\nu}_{\mathbf{q}} \gg K_B T$ and thus $n(\omega^{\nu}_{\mathbf{q}}) \sim 0$. Unless otherwise specified, the intensities are normalized to the maximum value of the $2D$ peak. In the following four subsections (and in Appendix B), we describe the model to obtain the DR scattering amplitudes K.

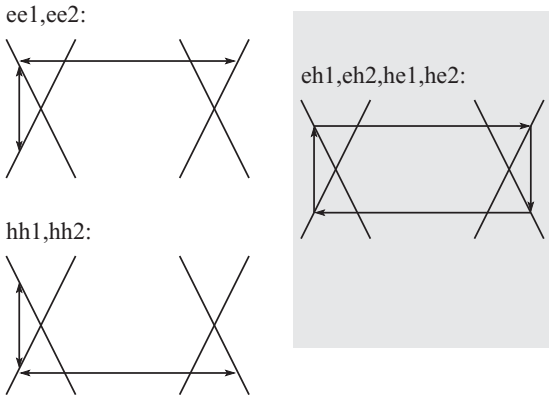

FIG. 2. An alternative representation (customary for graphene and graphite) of the processes associated to the diagrams of Fig. 1. The crosses represent the electronic dispersion near the conic region. The vertical arrows represent the electron/hole creation and recombination. The horizontal arrows represent the scattering with a defect or with a phonon. For simplicity we show only the processes involving a phonon with momentum along the **K**-**M** line. In this paper, the term "*ab* processes" refers to the processes highlighted by the gray area (*eh*1, *eh*2, *he*1, and *he*2). The other processes are referred to as "*aa* processes."

B. Electron and phonon dispersion

The electronic structure, $\epsilon^{\alpha}_{\mathbf{k}}$ and $|\mathbf{k},\alpha\rangle$, is obtained from a tight-binding (TB) model with one orthonormalized p_z orbital per site and interactions up to fifth neighbors (details are in Appendix B 1). We use $t_1 = -3.40$ eV, $t_2 = 0.33$ eV, $t_3 = -0.24$ eV, $t_4 = 0.12$ eV, and $t_5 = 0.09$ eV, where t_i is the ith neighbor hopping parameter. The resulting electronic dispersion is shown in Fig. 3. These TB parameters were obtained as follows:[24] first, the t_i are fitted to density-functional theory (DFT) electronic band dispersion to reproduce the $\pi - \pi^*$ bands along the **Γ**-**K**-**M** line; then, all the t_i are rescaled by $+18\%$ in order to reproduce the π-band slope near **K** from GW calculations, which are in excellent agreement with angle-resolved photoemission spectra (ARPES) measurements on graphite.[25]

We remark that, in the present context, a good description of the trigonal warping of the π band cone is very relevant, since the actual shape of the trigonal warping determines the $\mathbf{q}$ vectors of the phonons associated to the D line. The present five-neighbor TB can reproduce very well the trigonal warping as obtained from DFT. On the contrary, by using a first-neighbor TB model, the trigonal warping is underestimated. Another relevant characteristic, which is badly described by small-neighbor TBs, but which is well described by the present five-neighbor TB, is the electron/hole asymmetry $\epsilon^{\pi^*}_{\mathbf{k}} + \epsilon^{\pi}_{\mathbf{k}}$.

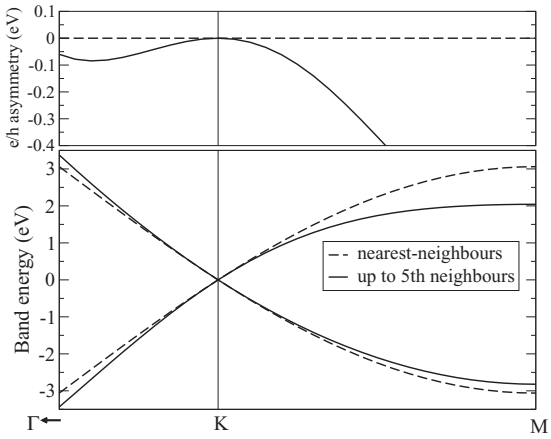

FIG. 3. Graphene electronic dispersion obtained with the five-neighbor tight binding described in the text (solid line). For a comparison we also show the dispersion obtained with the first-neighbor TB having the same Fermi velocity at **K** (dashed line). The electron/hole (e/h) asymmetry is defined as $\epsilon^{\pi^*}_{\mathbf{k}} + \epsilon^{\pi}_{\mathbf{k}}$ and is constant for the first-neighbor TB.

This quantity depends on the **k** direction and has values of the order of the electronic broadening (see Sec. II F): e.g., for the states in resonance with a laser of 2.4 eV, the asymmetry is about 40 and 100 meV along the **K**-**Γ** and the **K**-**M** direction, respectively (Fig. 3). On the contrary, in a first-neighbor TB model, the e/h asymmetry is **k** independent and it is equal to zero.

Phonon dispersions $\omega^{\nu}_{\mathbf{q}}$ are obtained from *ab initio* DFT calculations[26] corrected with GW as in Refs. 27 and 28. In particular, first we computed the DFT phonon dispersion, then we "correct" the dispersion of the highest optical branch near **K** (the branch that is TO near **Γ** and associated with the A'_1 mode at **K**; see Fig. 4) by rescaling the phonon self-energy contribution to the dynamical matrix consistently with the GW calculated electron-phonon coupling and electronic π band dispersion.[27] Calculations are done for graphene with the same computational details of Ref. 28. In Ref. 28, the rescaling factor is a constant, $r^{GW} = 1.61$, all over the Brillouin zone (BZ) and the phonons are studied just in the neighborhood of **K**. Here, in order to obtain a phonon dispersion all over the BZ, the rescaling factor $r^{GW}_{\mathbf{q}}$ depends on **q**. $r^{GW}_{\mathbf{q}} = r^{GW}$ near **K** and smoothly drops to 1 elsewhere:

$$r^{GW}_{\mathbf{q}} = 1 + (r^{GW} - 1)\frac{1}{2}\mathrm{erfc}\left(\frac{|\mathbf{q} - \mathbf{K^n}|\frac{a_0}{2\pi} - 0.2}{0.05}\right), \quad (6)$$

with a_0 the graphene lattice constant and $\mathbf{K^n}$ the nearest vector to **q** among those equivalent to **K**. The GW correction associated to r^{GW} changes the phonon slope of the highest optical branch near **K** by almost +60% (with respect to DFT) providing a much better agreement with measurements for graphite (Fig. 4). The precise value of the phonon dispersion near **K** is essential in the present context, since it determines the dependence of the D peak dispersion as a function of the exciting laser energy.[29]

Finally, notice that the present DFT calculations reproduce very well the experimental phonon dispersion from inelastic x-ray scattering (IXS) of Ref. 30 of the highest optical branch

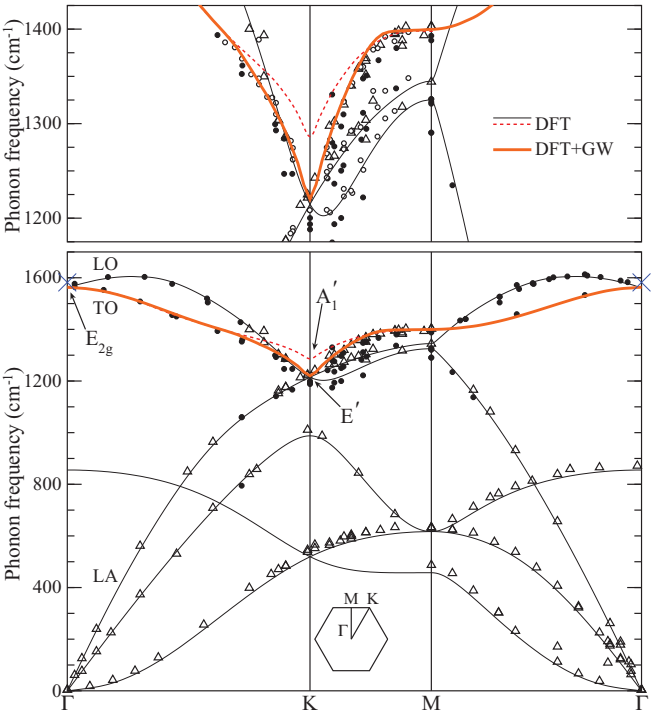

FIG. 4. (Color online) Calculated graphene phonon dispersion from DFT (lines) vs IXS measurements on graphite from Refs. 30 (filled dots), 31 (triangles), and 28 (open dots). The highest optical branch near **K** is "corrected" to include GW effects following Refs. 27 and 28, and is plotted with a thicker gray (red) line. The dashed line is the same branch calculated from standard DFT, without GW correction. The cross at **Γ** is the measured Raman G line frequency in graphite (1582 cm^{-1}).

near **Γ**. We can thus assume that the DFT frequency for the E_{2g} **Γ** mode (1561 cm^{-1}) is a precise fit of the IXS measurements. The 1561-cm^{-1} value is, however, 1.3% smaller than the measured frequency of the G Raman line of graphite, which is 1582 cm^{-1} (the corresponding infrared mode is 1586 cm^{-1}). This discrepancy between Raman and IXS measurements in graphite is so far unexplained.

C. Electron-phonon scattering

The electron-phonon scattering matrix elements $\Delta H_{\mathbf{q},\nu}$ are obtained from TB (explicit expressions are given in Appendix B 2) and depend on the parameter η_1, defined as the derivative of the nearest-neighbors hopping parameter with respect to the bond length. The present approach neglects the derivative of the hopping parameters (with respect to the atomic positions) for hopping computed for second and more distant neighbors. This approximation reproduces very well the **k** and **q** dependence of the electron-phonon matrix elements for electronic states with **k** near **K** and for optical phonons with **q** near **Γ** or near **K**. This was already verified in Ref. 32 by direct comparison with DFT calculations.

We define the average square of $\sqrt{2M\omega_{\mathbf{q}\nu}/\hbar}\Delta H_{\mathbf{q},\nu}$ between π and π^* at **K** as $\langle D^2_{\mathbf{\Gamma}}\rangle_F$ for the E_{2g} phonon at **Γ**. $\langle D^2_{\mathbf{K}}\rangle_F$ is the analogous quantity for the A'_1 phonon at **K**. From Eqs. (B4) and (B5) from Appendix B 1, after some algebra, $\langle D^2_{\mathbf{\Gamma}}\rangle_F = 9/4(\eta_1)^2$ and $\langle D^2_{\mathbf{K}}\rangle_F = 9/2(\eta_1)^2$ (η_1 is defined in the

previous paragraph and the notation is consistent with Ref. 27). It follows that, within TB, $\langle D^2_{\mathbf{K}}\rangle_F/\langle D^2_{\mathbf{\Gamma}}\rangle_F = 2$ (that is, this ratio does not depend on the actual value of the TB parameter η_1). This last relation is well reproduced by DFT calculations, within LDA or GGA, but not by GW ones (see Table I of Ref. 27). As a consequence, a single value for η_1 could be used to describe reasonably well the DFT electron-phonon interaction for phonons in all the Brillouin zone. On the contrary, we need two distinct values for η_1, $\eta_1^{\mathbf{\Gamma}} = 5.25$ eV/Å, and $\eta_1^{\mathbf{K}} = 6.55$ eV/Å, to reproduce the GW value of $\langle D^2_{\mathbf{K}}\rangle_F$ and $\langle D^2_{\mathbf{\Gamma}}\rangle_F$, respectively, from Table I of Ref. 27. Here we will use $\eta_1 = \eta_1^{\mathbf{\Gamma}}$ for phonons near $\mathbf{\Gamma}$ (those associated to the D' and $2D'$ lines), and $\eta_1 = \eta_1^{\mathbf{K}}$ for phonons near $\mathbf{K}$ (D, $2D$, and $D + D''$). A change of $\eta_1^{\mathbf{\Gamma}}$ and $\eta_1^{\mathbf{K}}$ values will affect the present calculations as a uniform intensity scaling of some peaks with respect to others.

D. Electron-light scattering

Explicit expressions for the D_{in} and D_{out} matrix elements are given in Appendix B 3. We assume that the polarization of the incoming and scattered light are on the graphene (x,y) plane. The computed Raman intensity $I_{i,o}$ depends on two indexes determined by the polarization of the incident ($i = x,y$) and of the scattered light ($o = x,y$). The polarizations are chosen so as to reproduce different kinds of Raman experiments. In the *parallel polarization* case, the incident and scattered light are parallel polarized and $I_{\parallel} = I_{xx} + I_{yy}$. In the *transverse polarization* case, the incident and scattered light are perpendicularly polarized and $I_{\perp} = I_{xy} + I_{yx}$. If the light is not polarized $I_{\text{unpol}} = I_{xx} + I_{yy} + I_{xy} + I_{yx}$. Unless specified differently calculations are done in the nonpolarized case. In Sec. III B 3, the effects of parallel and transverse light polarizations are discussed.

E. Electron-defect scattering

Defect scattering is treated within the Born approximation. Namely, the defect scattering operator H_D is the difference between the TB Hamiltonian in presence of the defect and that of the defect-free system. H_D is determined by considering three distinct kinds of defects.

(i) The *on-site defects*: defects that change the value of the on-site TB parameter by δV_0.

(ii) The *hopping defects*: change the value of one of the first-neighbor hopping TB parameters by δt_1.

(iii) The *Coulomb defects*: charged impurities adsorbed at a distance h from the graphene sheet that interact with graphene with a Coulomb potential. Following Ref. 33, we consider an environment dielectric constant $\kappa = 2.5$.

We remark that these are very simplified prototypical models and that a realistic description of a given type of impurity, which is beyond the present scope, will result in a combination of these three kinds of perturbations. However, it is reasonable to expect that the present three models describe the most important characteristics of a certain kind of defects. For instance, the on-site defect is the most simple description of a hydrogen atom bound to a carbon atom in the graphene sheet. Hopping defects are any defects that lead to deformations of the carbon-carbon bonds in graphene. A Coulomb defect describes any charged atom or molecule adsorbed over the graphene sheet. Explicit expressions of the three defect scattering operators H_D are given in Appendix B 4. The three models are characterized by the parameters δV_0, δt_1, and h, whose values will be specified in the discussion. The results will be expressed as a function of the defect concentration $n_d = N_d/A_0$, where $A_0 = \sqrt{3}/2a_0^2$ is the graphene unit-cell area, with $a_0 = 2.46$ Å the graphene lattice spacing.

Note that the Raman intensity of the defect-induced lines (e.g., D, D', and D'') is proportional to the average number of defects in the unit cell, N_d [Eq. (3)]. This is because the scattering from defects on different sites is considered as incoherent, which is reasonable for low defect concentrations. In particular, for on-site and hopping defects, the defect-induced intensities are proportional to $\alpha_{\text{on}} = n_d(\delta V_0)^2$ and to $\alpha_{\text{hopp}} = n_d(\delta t_1)^2$, with n_d the defect concentration. Through the text, we will specify the value of these parameters, in order to make meaningful the comparison of the defect-induced line intensities with those of the phonon-phonon lines (e.g., $2D$, $2D'$, and $D' + D''$).

F. Electronic linewidth

An electronic state $|\mathbf{k}\alpha\rangle$ ($\alpha = \pi^*$ or π) has a finite lifetime $\tau^{\alpha}_{\mathbf{k}}$ (which is associated to a line broadening energy $\gamma^{\alpha}_{\mathbf{k}} = \hbar/\tau^{\alpha}_{\mathbf{k}}$) because the electronic states interact, e.g., with phonons and with defects. The broadening energies $\gamma_{\mathbf{k}}$ in the denominators of the DR amplitudes K [e.g., in Eqs. (4) and (5)] are the sum of the broadenings of the corresponding electronic states. As examples, in both Eqs. (4) and (5), $\gamma^A_{\mathbf{k}} = \gamma^{\pi^*}_{\mathbf{k}} + \gamma^{\pi}_{\mathbf{k}}$, $\gamma^B_{\mathbf{k}} = \gamma^{\pi^*}_{\mathbf{k+q}} + \gamma^{\pi}_{\mathbf{k}}$, and $\gamma^C_{\mathbf{k}} = \gamma^{\pi^*}_{\mathbf{k}} + \gamma^{\pi}_{\mathbf{k}}$. For $\alpha = \pi^*$ or π, $\gamma^{\alpha}_{\mathbf{k}}$ is the full width at half maximum of the electron/hole spectral function as measured, e.g., by ARPES.

We consider γ as the sum of two contributions

$$\gamma^{\alpha}_{\mathbf{k}} = \gamma^{\alpha(ep)}_{\mathbf{k}} + \gamma^{\alpha(D)}_{\mathbf{k}}. \tag{7}$$

The first is due to electron-phonon scattering. It is an intrinsic broadening (present in perfectly crystalline samples) and, according to the golden rule, is

$$\gamma^{\alpha(ep)}_{\mathbf{k}} = \frac{2\pi}{N_q}\sum_{\mathbf{q},\nu} |\langle \mathbf{k}+\mathbf{q},\alpha|\Delta H_{\mathbf{q},\nu}|\mathbf{k},\alpha\rangle|^2 \times \delta\left(\varepsilon^{\alpha}_{\mathbf{k}} - \varepsilon^{\alpha}_{\mathbf{k+q}} - \hbar\omega^{\nu}_{-\mathbf{q}}\right), \tag{8}$$

where α refers to π or π^* bands, the sum is performed on a uniform grid of N_q $\mathbf{q}$ points in the Brillouin zone and on all the phonon branches ν. A good approximation of $\gamma^{\alpha(ep)}$ is obtained by considering conic bands ($|\epsilon| = \hbar v_F k$, being v_F the Fermi velocity) and only the two phonons E_{2g} at $\mathbf{\Gamma}$ and A'_1 at $\mathbf{K}$, with energies $\hbar\omega_{\mathbf{\Gamma}}$ and $\hbar\omega_{\mathbf{K}}$. By defining $\langle g^2_{\mathbf{\Gamma}}\rangle = \sqrt{\hbar/(2M\omega_{\mathbf{\Gamma}})}\langle D^2_{\mathbf{\Gamma}}\rangle_F$ and $\langle g^2_{\mathbf{K}}\rangle = \sqrt{\hbar/(2M\omega_{\mathbf{K}})}\langle D^2_{\mathbf{K}}\rangle_F$ (see Sec. II C), Eq. (8) becomes

$$\gamma^{\alpha(ep)}_{\text{conic}} = \frac{\pi}{2}\left[2\langle g^2_{\mathbf{\Gamma}}\rangle N_{\alpha}(|\epsilon| - \hbar\omega_{\mathbf{\Gamma}}) + \langle g^2_{\mathbf{K}}\rangle N_{\alpha}(|\epsilon| - \hbar\omega_{\mathbf{K}})\right],$$
$$N_{\alpha}(\epsilon) = \frac{\sqrt{3}}{\pi}\left(\frac{a_0}{\hbar v_F}\right)^2 |\epsilon|\theta(|\epsilon|), \tag{9}$$

where N_{α} is the electronic density of states of the $\alpha = \pi$ or π^* band, with a_0 the lattice spacing and $\theta(x)$ the Heaviside

step function. Using the parameters of the present work, $N_\alpha(\epsilon) = 0.079\,08\ eV^{-2}|\epsilon|\theta(|\epsilon|)$ and for $|\epsilon| > 0.196$ eV,

$$\gamma^{\alpha(ep)}_{\rm conic} = 41.89(|\epsilon| - 0.1645)\ \ {\rm meV}, \tag{10}$$

where ϵ is expressed in eV.

The second contribution in Eq. (7) is due to electron-defect elastic scattering. It is extrinsic (it is induced by the presence of impurities and depends on the sample quality) and is

$$\gamma^{\alpha(D)}_{\mathbf{k}} = N_d \frac{2\pi}{N'_k} \sum_{\mathbf{k}'} |\langle \mathbf{k}',\alpha|H_D|\mathbf{k},\alpha\rangle|^2 \delta\left(\epsilon^\alpha_{\mathbf{k}} - \epsilon^\alpha_{\mathbf{k}'}\right), \tag{11}$$

where the sum is performed on a uniform grid of N'_k $\mathbf{k}'$ points in the Brillouin zone. The electron-defect scattering operator H_D is defined as in Sec. II E and Appendix B 4 and depends on the considered kind of defect. N_d is the average number of defects in the unit cell.

Figure 5 shows $\gamma^{(ep)}$ and $\gamma^{(\rm D)}$ for on-site and hopping defects ($\gamma^{(\rm D)} = \gamma^{(\rm on)}$, or $\gamma^{(\rm D)} = \gamma^{(\rm hopp)}$). The γ in Fig. 5 are calculated with Eqs. (8) and (11) and are plotted as a function of the energy of the corresponding electronic state ($\epsilon^{\pi^*}_{\mathbf{k}}$ or $\epsilon^{\pi}_{\mathbf{k}}$). $\gamma^{(ep)}$ is compared with the conic-band results of Eq. (10). As expected, the two results are similar for energies smaller than 1 eV.

$\gamma^{(\rm on)}$ is univocally determined by the energy and, in Fig. 5, is represented by a line. $\gamma^{(\rm on)}$, in particular, is proportional to the density of states. A detailed analysis of the Coulomb case is discussed in Ref. 33. On the contrary, $\gamma^{(ep)}$ and $\gamma^{(\rm hopp)}$ display a dispersion associated to the fact that different $\mathbf{k}$ electronic states with the same energy can have a different lifetime. However, the dispersion is relatively small, and for the present purpose they will also be considered a function of the energy. All the contributions ($\gamma^{(ep)}$, $\gamma^{(\rm on)}$, and $\gamma^{(\rm hopp)}$) increase with energy and display a noticeable asymmetry between positive and negative energies due to the graphene electron/hole asymmetry.

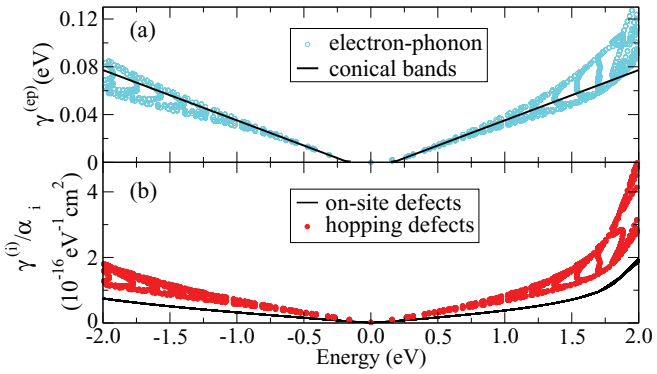

FIG. 5. (Color online) Electronic linewidth as a function of energy. (a) Contribution of electron-phonon scattering to the electronic linewidth, $\gamma^{(ep)}$, compared to conical bands results [Eq. (10)]. (b) Contribution of on-site and hopping impurity scattering to the electronic linewidth. $\gamma^{(\rm on)}$ is proportional to $\alpha_{\rm on} = n_d(\delta V_0)^2$ and $\gamma^{(\rm hopp)}$ is proportional to $\alpha_{\rm hopp} = n_d(\delta t_1)^2$ (Sec. II E). We thus plot $\gamma^{(\rm i)}/\alpha_i$, where the label "i" refers to "on" (on-site defect) or to "hopp" (hopping defect).

In actual calculations [e.g., in Eqs. (4) and ((5)] we neglect the dependence on $\mathbf{k}$ and we use

$$\gamma^A_{\mathbf{k}} = \gamma^B_{\mathbf{k}} = \gamma^C_{\mathbf{k}} = \gamma^{\rm tot}, \tag{12}$$

where $\gamma^{\rm tot}$ depends only on the excitation energy ϵ_L, on the kind of defect D, and on its concentration n_D, through

$$\gamma^{\rm tot} = \tilde\gamma^{(ep)}(\epsilon_L) + \tilde\gamma^{(D)}(\epsilon_L, n_D). \tag{13}$$

$\tilde\gamma$ are the sum of the two contributions for π an π^* bands in a small energy range close to half the excitation energy ϵ_L. As an example, $\tilde\gamma^{(ep)} = \overline{\gamma}^{(ep)}(\epsilon_L/2) + \overline{\gamma}^{(ep)}(-\epsilon_L/2)$, where $\overline{\gamma}^{(ep)}(\epsilon)$ is the average of $\gamma^{(ep)}$ from Fig. 5 at that energy, in particular, for $\epsilon_L \gtrsim 1.0$ eV,

$$\tilde\gamma^{(ep)}(\epsilon_L) = \left(18.88\epsilon_L + 6.802\epsilon_L^2\right)\ {\rm meV}, \tag{14}$$

where ϵ_L is expressed in eV. While comparing these values with literature, notice that $\gamma^{(\rm tot)}$ and the $\tilde\gamma$'s correspond to the sum of the width of electrons and holes and are thus roughly two times bigger than the width of electronic states. To give some examples, for $\epsilon_L = 2.4$ eV, and for the typical defect concentrations of the present work, $\alpha_{\rm on} = \alpha_{\rm hopp} = 6.4 \times 10^{13}$ eV^2 cm^{-2}, $\tilde\gamma^{(\rm on)} = 5$ meV, and $\tilde\gamma^{(\rm hopp)} = 12$ meV. On the other hand, for $\epsilon_L = 2.4$ eV, $\tilde\gamma^{(ep)} = 84$ meV is the dominant contribution and, in several cases, we will just consider $\gamma^{\rm tot} \sim \tilde\gamma^{(ep)}$. Similar values of $\gamma^{\rm tot} \sim \tilde\gamma^{(ep)}$ have been extracted from measurements in Ref. 34 (note that $\gamma_{\rm e-ph}$ of Ref. 34 corresponds to $\tilde\gamma^{(ep)}/4$ in the present notation).

Finally, in charged graphene a further contribution to the broadening due to electron-electron interaction[34] can be relevant when $0.06|\epsilon_F| \gtrsim \tilde\gamma^{(ep)}/4$ where ϵ_F is the Fermi energy [see, e.g., Eq. (8) of Ref. 34]. For electron/hole concentrations of the order of 10^{12} cm^{-2} this contribution is negligible and, here, it is not considered.

III. RESULTS AND DISCUSSION

This section presents the calculation of the double-resonant (DR) Raman spectra of graphene and discuss the results. Section III A describes the overall agreement with measurements. Section III B describes the dependence of the spectra on excitation energy and light polarization. Section III C describes the dependence of the Raman intensities on various parameters such as the electronic linewidth, the excitation energy, and the defect concentration. Section III D describes the dependence of the spectra on the type of defect. Section III E is dedicated to the interpretation of the results. It is focused on some specific issues such as the determination of the most relevant processes and phonons, the role of quantum interference, and on the interpretation of the small width of the main DR Raman lines.

A. Overall agreement with measurements

Figures 6 and 7 compare the present calculations with Raman spectra of Refs. 11 and 1, for an excitation energy $\epsilon_L = 2.4$ eV. In Fig. 6, below 2000 cm^{-1} the processes are due to phonon-defect scattering and calculations are done considering only the hopping defects (this choice is justified in Sec. III D), using the parameter $\alpha_{\rm hopp} = 6.4 \times 10^{13}$ eV^2 cm^{-2} (see Sec. II E), which reproduces the measured ratio of the integrated areas between D and $2D$ lines of Ref. 11. Above

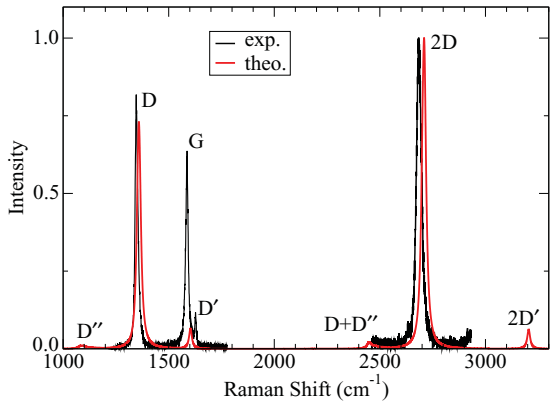

FIG. 6. (Color online) Intensity vs Raman shift for $\varepsilon_L = 2.4$ eV. Comparison of the present calculations with the measurements from Ref. 11. Notice that our model includes only double-resonant processes and thus the G line is not present. Measurements correspond to a defect concentration $n_d = 10^{12}$ cm^{-2}. Calculations are done using $\gamma^{\rm tot} = 96$ meV, and hopping defects with $\alpha_{\rm hopp} = 6.4 \times 10^{13}$ eV^2 cm^{-2}. All the intensities are normalized to the maximum value of the $2D$ line.

2000 cm^{-1}, all the processes are due to two-phonon scattering. We remark that the G line is a single-resonant process, which is not included in the present calculations.

The agreement between calculations and measurements is extremely good. In particular, all the lines observed experimentally, even the small intensity ones, are present in the calculated spectra and the relative intensities among phonon-defect lines (such as the D and the D') or among two-phonon lines (such as $2D$, $2D'$, or $D + D''$) are correctly reproduced. The most remarkable agreement relates to the linewidths. Indeed, the present model reproduces very well the measured small widths of the D, D', $2D$, and $2D'$ lines. Moreover, the model reproduces quite well the symmetric Lorentzian shapes of the $2D$ and $2D'$ lines and the asymmetric shape of $D + D''$ band. We remark that, in the present model, the only parameter used to fit the Raman data is $\alpha_{\rm hopp}$. This

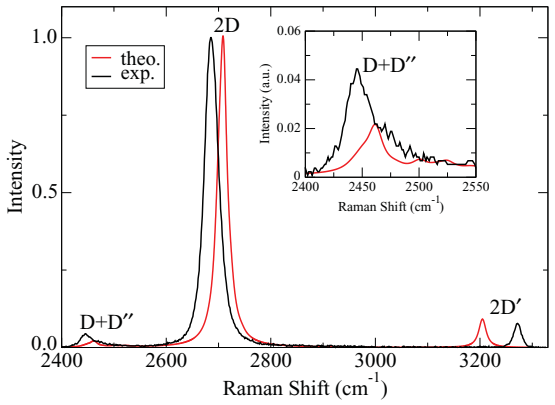

FIG. 7. (Color online) Intensity vs Raman shift for $\varepsilon_L = 2.4$ eV. Comparison of the present calculations with the measurements from Ref. 1. The figure reports only two-phonon processes. Calculations are done using $\gamma^{\rm tot} = 84$ meV. All the intensities are normalized to the maximum value of the $2D$ line. The inset shows the D+D'' band in a different scale.

parameter determines the ratio of the D versus $2D$ intensities but does not affect the relative intensities among phonon-defect or among two-phonon lines, the width of the lines, and their shape.

As far as the line frequencies are concerned, calculations and measurements display some small deviations of the order of a few meV. We remark that the line frequencies are determined by a subtle interplay between the phononic and electronic energy dispersions, and that the present dispersions are obtained from state-of-the-art *ab initio* computational methods, which correctly reproduce ARPES and IXS measurements (Sec. II B). A correction of the electronic or of the phononic dispersions, to reproduce with more precision the Raman frequencies, would be done at the expense of introducing fitting parameters to the model, which is beyond the present scope.

B. Dependence of the spectra on the laser

This section describes the dependence of the spectra on excitation energy and light polarization. Excitation energies vary from 1.2 to 4.0 eV, which are energies mainly used in actual experiments.

1. *Dependence of the main lines on the excitation energy*

Figure 8 displays the calculated spectra of the main double-resonant Raman lines for three different excitation energies. In all cases, we use the electronic broadening $\gamma^{\rm tot} = \tilde{\gamma}^{(ep)}$, calculated at the corresponding excitation energy (Sec. II F). In general, by increasing the excitation energy, the bands become broader and the relative intensities change. The behavior of the $2D$ line is particularly interesting. At $\epsilon_L = 2.4$ eV, the $2D$ line presents a Lorentzian line shape with a relatively small linewidth, while at $\epsilon_L = 3.8$ eV, it is much broader showing two components with smaller, $2D^-$, and higher, $2D^+$ Raman shifts, as discussed in detail in Sec. III E 4. Here, we just remark that the presence of a small width $2D$ line with Lorentzian shape is commonly used to detect a graphene monolayer in samples containing flakes with a different number of graphene layers.[1] According to Fig. 8, this kind of experiment makes

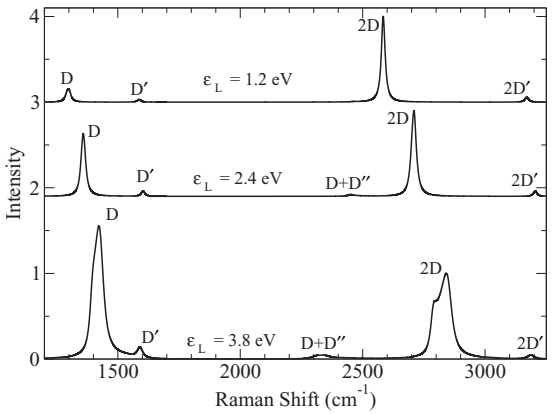

FIG. 8. Calculated Raman spectra for $\varepsilon_L = 1.2$ eV and $\gamma^{\rm tot} = 32$ meV, $\varepsilon_L = 2.4$ eV and $\gamma^{\rm tot} = 84$ meV, $\varepsilon_L = 3.8$ eV and $\gamma^{\rm tot} = 170$ meV. Calculations are done using hopping defects with $\alpha_{\rm hopp} = 6.4 \times 10^{13}$ eV^2 cm^{-2}. All the intensities are normalized to the corresponding $2D$ line maxima.

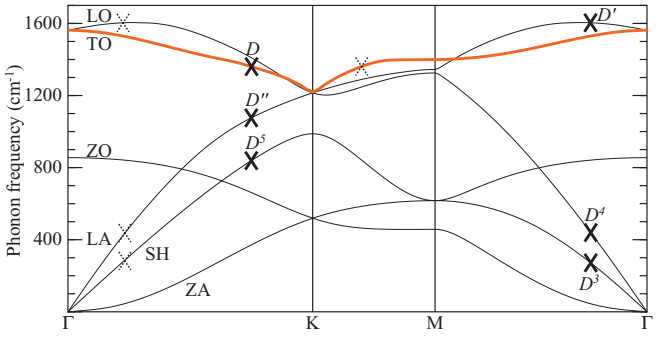

FIG. 9. (Color online) Phonon dispersion of graphene along high-symmetry lines. Bold crosses indicate the phonons that mostly contribute to the D, D', D'', D^3, D^4, and D^5 Raman bands, for $\epsilon_L = 2.4$ eV. Dotted crosses indicate phonons that also contribute to the D, D', D^3, and D^4 bands but with smaller intensity. The crosses are determined from the maximum of $\mathcal{I}_{\mathbf{q}}$ as defined in Sec. III B 2.

sense only when it is done at $\epsilon_L \lesssim 2.4$ eV, but not at higher excitation energies.

Figure 9 shows the wave vector and the branch of the high-symmetry phonons, which mostly contribute to the DR graphene lines, for $\epsilon_L = 2.4$ eV. The figure display the phonons associated with the single-phonon Raman lines D, D', D'', D^3, D^4, and D^5, where D^3, D^4, and D^5 refer to the small intensity lines of Fig. 11. The D line is associated to the phonon branch affected by the Kohn anomaly (thick gray line in Fig. 4). This branch, near $\mathbf{\Gamma}$, becomes almost transverse (TO). The D' line is associated to the branch which, near $\mathbf{\Gamma}$, is almost longitudinal (LO). The two-phonon bands, such as the $2D$, $2D'$, and $D + D''$ are associated with the emission of two phonons which, in the scale of Fig. 9, are almost indistinguishable from those of the D, D', and D'' lines.

Figure 10 shows the calculated shift of the main Raman lines as a function of the excitation energy, ϵ_L. The Raman shift of the D and $2D$ lines increases with increasing laser energy. The D' Raman shift does not show a monotonic behavior but it does not change significantly. The $D + D''$ Raman shift is

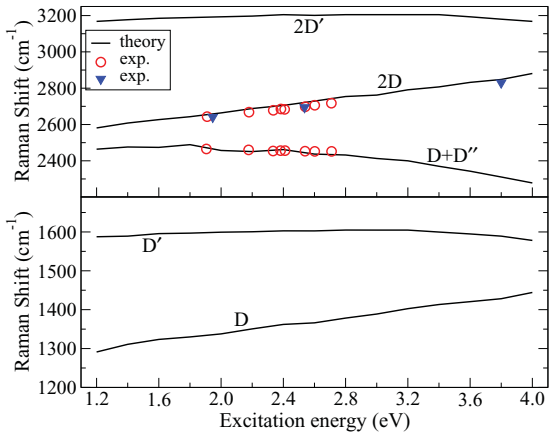

FIG. 10. (Color online) Raman shift as a function of excitation energy. Upper panel: two-phonon bands. Lower panel: disorder-induced bands. Our results compared to experimental data from Refs. 9 (circles) and 35 (triangles).

almost constant for ϵ_L between 1.2 and 1.8 eV, and decreases for $\epsilon_L \gtrsim 1.8$ eV. Figure 10 also shows the experimental data from Ref. 9 for the $2D$ and $D + D''$ lines and from Ref. 35 for the $2D$ line. The good agreement with measurements is not surprising since the dispersion of a DR line as a function of ϵ_L is determined by the phonon dispersion and in Ref. 27 it was already shown that the present phonon dispersions (obtained from DFT plus GW corrections) reproduce the measured D line shift as a function of ϵ_L. The behavior of the shift as a function of ϵ_L is easily understood by comparing with the phonon dispersions in Fig. 9. For instance, for the D line, when the excitation energy increases, the phonons mostly involved in the DR process move away from **K**, and their frequencies are higher. The same reasoning explains the behavior of the D' frequency. For the two-phonon lines, one has to consider the frequencies of the two phonons involved. For instance, the $2D$ line Raman shifts are twice as large as the D ones. For the $D + D''$ line, the energy of one phonon branch increases, while the other decreases while moving away from **K**.

2. *Small intensity bands*

The calculated spectra display some small intensity bands, which are shown in Fig. 11. Some of these bands are extremely weak and it is not clear whether they could be possibly measured, on the other hand the D'' is observed[7,11] and the bands that we label as $D' + D^4$ and $D' + D^3$ have been measured recently.[36,37] Figure 12 reports the shift of these small intensity bands as a function of the excitation energy. The agreement with available measurements is good. Figure 9 reports the high-symmetry phonons associated with the bands that we label as D^3, D^4, D^5, and D''. The D^3 and D^4 bands are associated with phonons near $\mathbf{\Gamma}$, which have a momentum very similar to the momentum of the phonons associated to the D' line. The D^5 and D'' bands are associated with phonons near **K**, with a momentum very similar to the momentum of the D phonons. The D^3, D^4, D^5, and D'' bands are, however, much weaker than the D and D' ones, because the electron-phonon

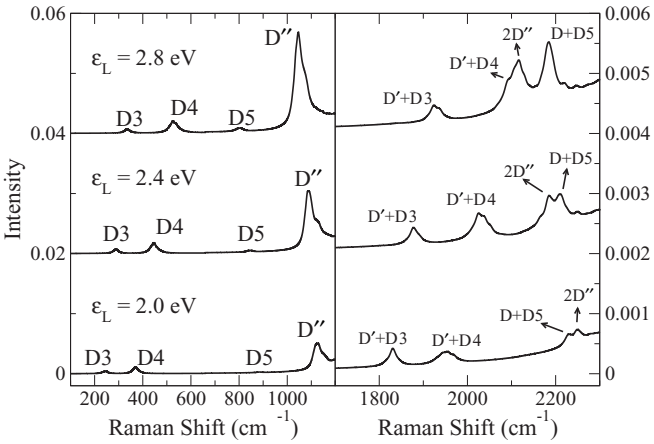

FIG. 11. Calculated Raman spectra for small intensity bands. Calculations are done using $\epsilon_L = 2.0$ eV and $\gamma^{\text{tot}} = 65$ meV (upper), $\epsilon_L = 2.4$ eV and $\gamma^{\text{tot}} = 84$ meV (middle), $\epsilon_L = 2.8$ eV and $\gamma^{\text{tot}} = 106$ meV (lower). We consider hopping defects with $\alpha_{\text{hopp}} = 6.4 \times 10^{13}$ eV^2 cm^{-2}. All the intensities are normalized to the corresponding $2D$ line maxima.

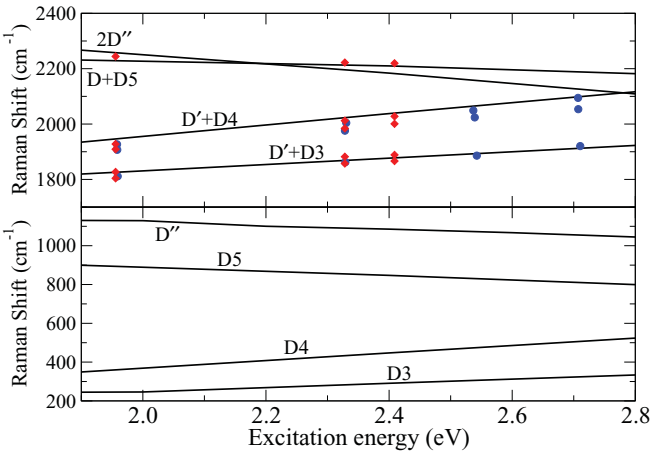

FIG. 12. (Color online) Raman shift vs excitation energy for the small intensity bands of Fig. 11. Upper and lower panels display results for two-phonon and defect-induced bands, respectively. Upper panel calculations are compared with measurements from Refs. 36 (dots) and 37 (diamonds).

coupling (between π electronic bands) for those branches is much weaker than the one of the D and D' (see Ref. 32).

3. *Dependence on the light polarization*

So far, we have shown calculations done with unpolarized light. We now discuss how the results are affected by the use of polarized light. For parallel and transverse polarizations, we calculated $I_{\parallel}$ and $I_{\perp}$ as defined in Sec. II D. Figure 13 compares the results obtained for $\epsilon_L = 2.4$ eV and $\epsilon_L = 3.8$ eV. The intensity in the parallel polarization case is considerably larger than in the transverse one, as expected. For $\varepsilon_L = 2.4$ eV, the spectrum shape almost does not depend on the polarization and the ratio $I_{\parallel}/I_{\perp}$ is about 2.7, in reasonable agreement with measurements in graphite,[38] graphene,[39] and earlier theoretical predictions.[16] For $\epsilon_L = 3.8$ eV, the D and $2D$ bands split into two components (see Sec. III E 4 for a detailed discussion) and the intensity ratio between the two components depends on the polarization. For example, the intensities of the two components of the $2D$ band, $2D^+$ and $2D^-$, are very similar within transverse polarization, while the $2D^+$ intensity is slightly higher than the $2D^-$ one, within parallel polarization. This finding is very remarkable since it could lead to measurable effects.

C. Dependence of the Raman intensities on the various parameters

In this section we discuss how the intensity of the main DR Raman lines is affected by the various parameters such as the electronic linewidth (Sec. III C 1), the excitation energy (Sec. III C 2), and the defect concentration (Sec. III C 3). In general, the absolute value of the intensities is affected by these parameters, however, we will mainly focus on how the ratio of the intensities of different lines is affected, since this last quantity can be measured more easily.

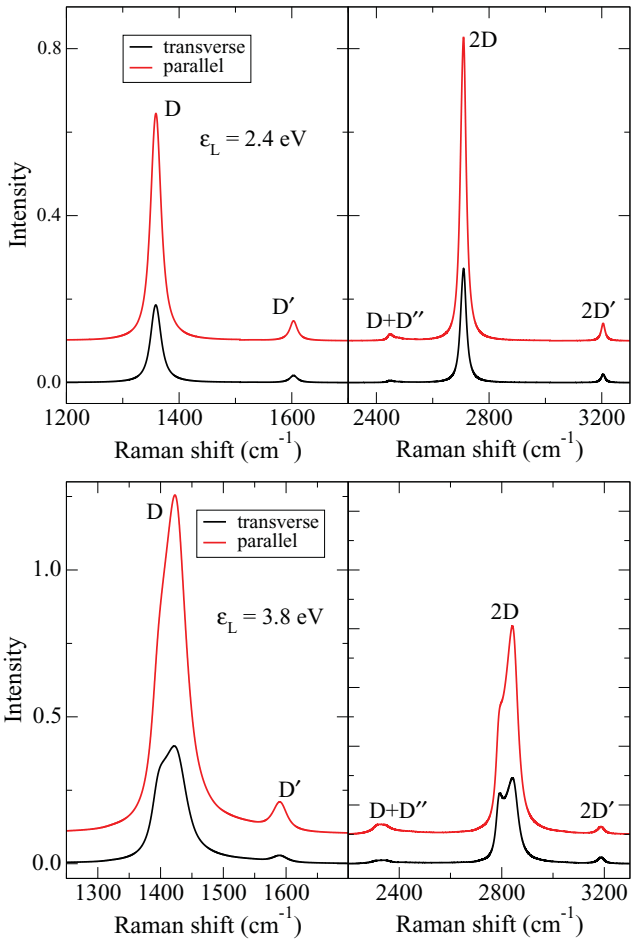

FIG. 13. (Color online) Comparison of calculated Raman spectra done with different light polarizations. Calculations are done using $\epsilon_L = 2.4$ eV and $\gamma^{\rm tot} = 84$ meV (upper plot), or $\epsilon_L = 3.8$ eV and $\gamma^{\rm tot} = 170$ meV (lower plot). We used hopping defects with $\alpha_{\rm hopp} = 6.4 \times 10^{13}$ eV^2 cm^{-2}. The intensities are normalized to the corresponding $2D$ line maxima calculated with unpolarized light. "Parallel" and "transverse" refer to $I_{\parallel}$ and $I_{\perp}$ as defined in Sec. II D.

1. *Dependence on the electronic broadening*

As already discussed in Sec. II F, the broadening parameter $\gamma^{\rm tot}$ [the sum of the electron and hole linewidths; see Eq. (12)] results from an intrinsic component (due to electron-phonon scattering), which depends on the laser energy, and from an extrinsic component, which increases by increasing the defect concentration. Eventually, in charged (doped) graphene, a further contribution due to electron-electron scattering can be relevant. The actual value of $\gamma^{\rm tot}$, which depends on the defect concentration, determines in a measurable way also the intensities of the two-phonon lines (which are not defect induced). Indeed, Fig. 14 reports the integrated areas under the $2D, 2D'$, and $D + D''$ lines [$A(2D)$, $A(2D')$, and $A(D + D'')$], as a function of $\gamma^{\rm tot}$. The areas of these lines decrease by increasing $\gamma^{\rm tot}$. In general, for all Raman lines studied here, the intensity decreases when the electronic linewidth increases, at fixed defect concentration. This is because, in Eq. (1), an increase of the imaginary values $i\gamma$ tends to kill the double-resonance condition.

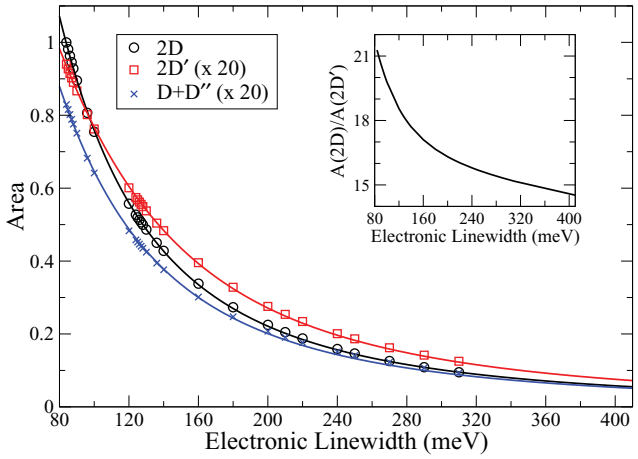

FIG. 14. (Color online) Integrated areas under the $2D$, $2D'$, and $D+D''$ lines [$A(2D)$, $A(2D')$, and $A(D+D'')$] as a function of the electron + hole linewidth ($\gamma^{\rm tot}$), for $\varepsilon_L = 2.4$ eV. The areas are normalized to $A(2D)$ calculated with $\gamma^{\rm tot} = \tilde{\gamma}^{(ep)} = 84$ meV. For clarity, $A(2D')$ and $A(D+D'')$ are multiplied by 20. Symbols are calculations, lines are the fit from Eq. (15). Inset: $A(2D)/A(2D')$ ratio.

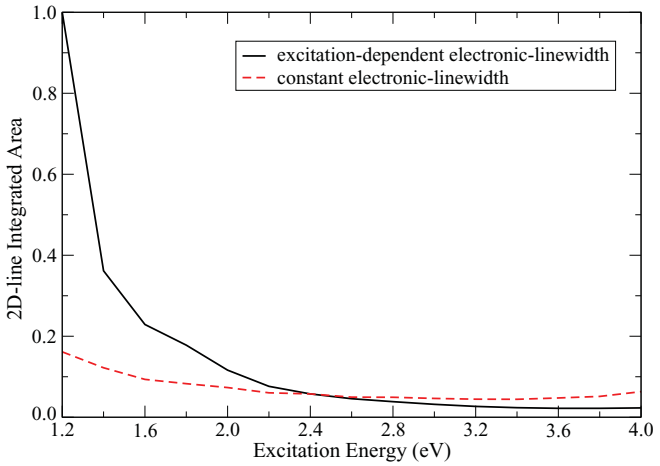

FIG. 15. (Color online) Integrated area under the $2D$ line as a function of the excitation energy ϵ_L. The defect concentration is zero. The full line is obtained by including the dependence of the broadening on ϵ_L, $\gamma^{\rm tot} = \tilde{\gamma}^{(ep)}(\epsilon_L)$ (see Sec. II F). The dashed line is from an unrealistic simulation in which $\gamma^{\rm tot}$ has been kept fixed to a constant value $\gamma^{\rm tot} = \tilde{\gamma}^{(ep)}(2.4\text{eV}) = 84$ meV, independent from ϵ_L.

It is interesting to notice that also the ratio of the two areas, $A(2D)/A(2D')$, depends on $\gamma^{\rm tot}$ (inset of Fig. 14). This result is particularly appealing since the ratio of the two areas can be measured in a relatively easy way. The measured value of $A(2D)/A(2D')$ compared to the inset of Fig. 14 (which is obtained for $\epsilon_L = 2.4$ eV) could thus be used to determine experimentally the electron+hole linewidth $\gamma^{\rm tot}$ and, in particular, its components due to defects and/or to electron-electron scattering in doped samples (keeping in mind that for large doping the value of the electron-phonon interaction itself is expected to change[40] and thus the inset of Fig. 14 cannot be used as it is). For $\gamma^{\rm tot} = \tilde{\gamma}^{(ep)} = 84$ meV, which is suitable for comparison with pristine graphene, $A(2D)/A(2D') = 21.5$, in agreement with experimental works that reported $A(2D)/A(2D')$ as being 27 (Ref. 1) and 26 ± 3.[41]

In Ref. 23 it has been shown that, if the electronic bands can be considered conic, the dependence of $A(2D)$ and $A(2D')$ on $\gamma^{\rm tot}$ should be $A = A_0/(\gamma^{\rm tot})^2$, where A_0 is a constant. This functional form, however, cannot be used for a quantitative description of the present results. Indeed, the integrated areas as a function of $\gamma^{\rm tot}$ reported in Fig. 14 can be fitted by a similar, but different, law:

$$\begin{aligned} A(2D) &= 9374/\left[(\gamma^{\rm tot})^2 + 48.5^2\right], \\ A(2D') &= 629/\left[(\gamma^{\rm tot})^2 + 80.0^2\right], \\ A(D+D'') &= 438/[(\gamma^{\rm tot})^2 + 59.6^2], \end{aligned} \tag{15}$$

where $\gamma^{\rm tot}$ is expressed in meV. An explanation of the discrepancy between Eqs. (15) and the model of Ref. 23 (which is based on a simplified description of the electronic bands) is probably associated to the importance of a proper inclusion of the trigonal warping and of the electron/hole asymmetry in the description of the electronic bands (Sec. II B). Another result of Ref. 23 is that

$$A(2D)/A(2D') = 2\left(\eta_1^{\mathbf{K}}/\eta_1^{\mathbf{\Gamma}}\right)^4 \times (\omega_{2D'}/\omega_{2D})^2. \tag{16}$$

Equation (16) is obtained by rewriting the equation in the last paragraph of Ref. 23 using the notation of Sec. II C and considering ω_{2D} and $\omega_{2D'}$ are the frequencies associated with the two Raman lines. Indeed, for large $\gamma^{\rm tot}$, the ratio $A(2D)/A(2D')$ from Eqs. (15) does not depend on $\gamma^{\rm tot}$. However, using the parameters of the present work, Eq. (16), gives $A(2D)/A(2D') = 6.8$, which is almost two times smaller than $A(2D)/A(2D') = 14.7$ obtained from the limit $\gamma^{\rm tot} \to \infty$ of Eqs. (15). This second discrepancy with the model of Ref. 23 is so far unexplained, since in this limit the effect of electron-hole asymmetry should become negligible. We also remark that the model of Ref. 23 predicts that the ratio $A(2D)/A(2D')$ does not depend on the excitation energy ϵ_L. In the following we will show that, on the contrary, $A(2D)/A(2D')$ strongly depends on ϵ_L.

2. *Dependence on the excitation energy*

The intensity of the $2D$ line decreases by increasing the excitation energy ϵ_L (Fig. 15). The most important contribution to the decrease comes from the fact that the electron/hole broadening $\gamma^{\rm tot}$ increases by increasing ϵ_L. This can be deduced from Fig. 15, which also shows the results for a fictitious system in which $\gamma^{\rm tot}$ is kept to a fixed value independent from ϵ_L. Indeed, in this second case, the dependence of $A(2D)$ on ϵ_L is much less marked than in the full calculation.

Figure 16(a) reports the calculated ratio of the integrated areas under the bands, $A(2D')/A(2D)$ and $A(D+D'')/A(2D)$, as a function of the excitation energy ϵ_L. These ratios considerably change in the range of excitation energies of the figure. $A(2D')/A(2D)$ decreases and $A(D+D'')/A(2D)$ increases rapidly. The values calculated for $\epsilon_L = 2.4$ eV compare reasonably well with those obtained from the measurements of Ref. 1. In the last paragraph of Sec. III C 1 we discussed the model of Ref. 23, which was used to theoretically determine the ratio $A(2D')/A(2D)$. The simplified model of Ref. 23 predicts that the ratio $A(2D')/A(2D)$ does not depend on ϵ_L. On the

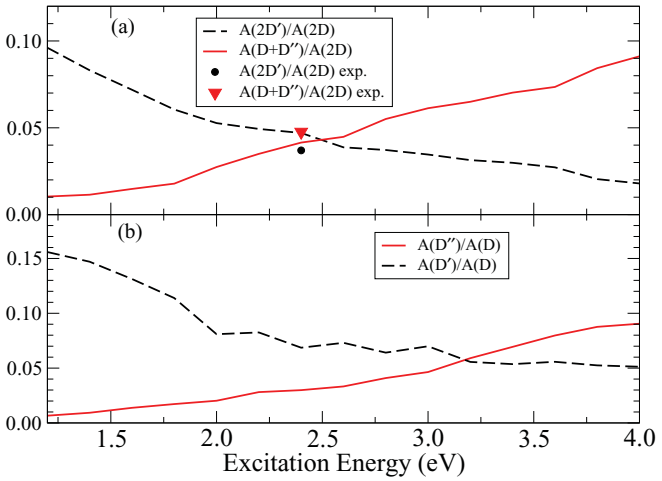

FIG. 16. (Color online) Ratio of the integrated areas under Raman bands as a function of excitation energy. (a) Two-phonon bands: our results compared to experimental data from Ref. 1. (b) Disorder-induced bands from hopping impurities, with $\alpha_{\text{hopp}} = 6.4 \times 10^{13}$ eV^2 cm^{-2}.

contrary, from Fig. 16(a), this dependence is very important. Using Eq. (16) (which is adapted from Ref. 23) and using, for consistency, the parameters of the present work, one obtains $A(2D')/A(2D) = 0.15$. This value is significantly higher than 0.09, which we obtain for the smallest ϵ_L of Fig. 16(a).

Figure 16(b) reports the ratio of the integrated areas under the defect-induced bands, $A(D')/A(D)$ and $A(D'')/A(D)$. Here, we consider again only hopping impurities. We also remark that the present approach is expected to be valid in the limit of small defect concentration. For small excitation energies the D''-band intensity is very small in comparison to the D one. For larger excitation energies the D'' relative intensity increases, reaching $A(D'')/A(D) = 0.09$ when $\epsilon_L = 4.0$ eV. On the other hand, the intensity of the D' band compared to the D band decreases by increasing the excitation energy. For ϵ_L up to about 3.0 eV the D' band is more intense than the D'' band, while for $\epsilon_L \gtrsim 3.2$ eV, the D'' is slightly more intense than the D'.

3. *Dependence on the defect concentration*

We now discuss how the intensities of the Raman bands are affected by defect concentration n_d. We recall that two-phonon Raman lines (such as the $2D$) depend on n_d only through the electronic broadening parameter γ^{tot} [Eq. (12)]. γ^{tot} is given by the sum of an intrinsic component $\tilde{\gamma}^{(ep)}$ (due to the electron-phonon interaction) and an extrinsic defect-induced component $\tilde{\gamma}^{(D)}$, which increases linearly by increasing n_d [Eq. (13)]. On the other hand, the defect-induced Raman lines (such as the D line) depend on n_d through two distinct mechanisms. First, it depends on n_d through γ^{tot} as for the two-phonon lines. Second, there is a proportionality factor between the Raman intensity and the number of defects in the sample [$I \propto N_d$ in Eq. (3)]. Basically, for a higher number of defects there are more scattering events that can activate the defect-induced lines, which, in crystalline samples, are not Raman active. In the following discussion, we will consider only hopping defects. As already shown in Secs. II E and II F, the calculated

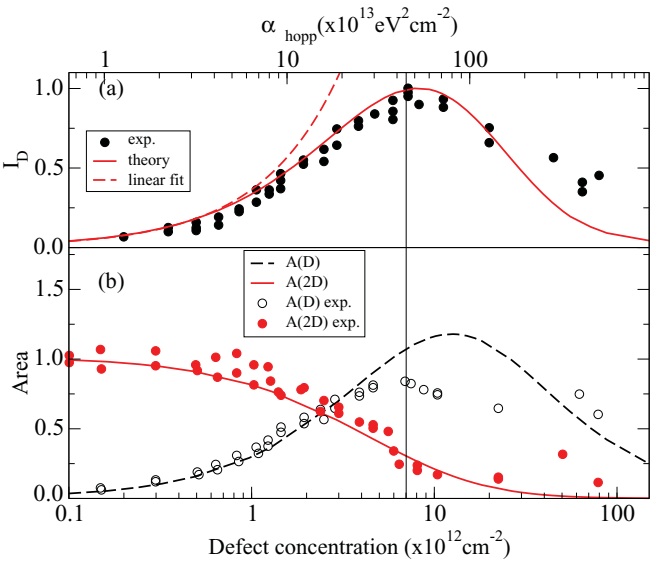

FIG. 17. (Color online) Intensity of the D and $2D$ Raman lines as a function of the defect concentration for $\epsilon_L = 2.4$ eV. Calculations are done using hopping defects and are reported as a function of the parameter $\alpha_{\text{hopp}} = n_d(\delta t_1)^2$ (n_d is the defect concentration and δt_1 is the hopping parameter), in the upper horizontal scale. The lower horizontal scale is obtained by considering $\delta t_1 = 8.0$ eV. (a) I_D is the maximum of the intensity of the D line; symbols are experimental data from Ref. 7. The dashed line is a linear fit of the I_D calculated values for $n_d < 5 \times 10^{11}$ cm^{-2}. Theoretical and experimental intensities have been normalized by their maximum values. (b) Integrated areas under D and $2D$ bands, $A(D)$ and $A(2D)$. Experimental data are from Ref. 11. Theoretical and experimental areas are normalized by $A(2D)$ at minimum defect concentration. The vertical line indicates the defect concentration of 7×10^{12} cm^{-2} ($\alpha_{\text{hopp}} = 4.5 \times 10^{14}$ cm^{-2} eV^2) for which the two contributions to the electronic broadening are equal: $\tilde{\gamma}^{(D)} = \tilde{\gamma}^{(ep)}$.

Raman spectra depend on the defect concentration n_d only through the parameter $\alpha_{\text{hopp}} = n_d(\delta t_1)^2$, with δt_1 the hopping parameter.

Figure 17 reports the D line peak maximum (I_D) and the integrated areas under the calculated $2D$ and D lines, $A(D)$ and $A(2D)$, as a function of the parameter α_{hopp}, for $\epsilon_L = 2.4$ eV. For $\alpha_{\text{hopp}} = 4.5 \times 10^{14}$ cm^{-2} eV^2, the two contributions to the broadening are equal, $\tilde{\gamma}^{(D)} = \tilde{\gamma}^{(ep)}$. The corresponding α_{hopp} is indicated in Fig. 17 with a vertical line. The intensity of the $2D$ line (which corresponds to a two-phonon process) monotonously decreases by increasing the defect concentration. For small defect concentrations ($\alpha_{\text{hopp}} \leqslant 10^{14}$ cm^{-2} eV^2) $\tilde{\gamma}^{(D)} \ll \tilde{\gamma}^{(ep)}$, $\gamma^{\text{tot}} \sim \tilde{\gamma}^{(ep)}$ slightly depends on the defect concentration, and $A(2D)$ is almost constant. For higher defect concentrations, $\tilde{\gamma}^{(D)}$ becomes the dominant contribution to γ^{tot}, which, as a consequence, becomes more sensitive to the defect concentration. The increase of γ^{tot} by increasing the defect concentration is associated to a decrease of $A(2D)$, because of the mechanism discussed in Sec. III C 1.

The intensity of the D line (which is a defect-induced process) has a different behavior. For low defect concentrations, it increases almost linearly, then it reaches a maximum, and finally decreases. This behavior results from the interplay of two competing mechanisms. For small defect concentration

$\tilde{\gamma}^{(D)} \ll \tilde{\gamma}^{(ep)}$ and $\gamma^{\rm tot} \sim \tilde{\gamma}^{(ep)}$. In this region, the intensity is expected to increase linearly [$I \propto N_d$ in Eq. (3)]. Indeed, the calculated intensity is well reproduced by a linear fit up to $\alpha_{\rm hopp} \leqslant 10^{14}$ cm^{-2} eV^2 (compare the continuous line with the dashed one in Fig. 17, upper panel). For $\alpha_{\rm hopp} > 4.5 \times 10^{14}$ cm^{-2} eV^2, the dependence of the broadening $\gamma^{\rm tot}$ on the defect concentration becomes the dominant mechanism, leading to a decrease of the intensity as for the $2D$ line. It is remarkable that the defect concentration for which $\alpha_{\rm hopp} = 4.5 \times 10^{14}$ cm^{-2} eV^2 (vertical line in Fig. 17) almost coincides with the maximum value reached by the D intensity I_D.

Figure 17 compares calculations with the intensities of the D and $2D$ measured in Refs. 11 and 7 as a function of the defect concentration. So far, we have discussed theoretical results as a function of $\alpha_{\rm hopp} = n_d(\delta t_1)^2$. $\alpha_{\rm hopp}$ defines the upper horizontal scale in Fig. 17. To make the comparison with measurements we need to attribute a value to the hopping energy δt_1. The best fit to measurements is obtained for $\delta t_1 = 8.0$ eV. This value is used only to rescale the horizontal axis of Fig. 17 and defines the defect concentration as reported in the lower horizontal axis of Fig. 17. The measured behavior as a function of the defect concentration is well reproduce by calculations. It is remarkable that the same value $\delta t_1 = 8.0$ eV can be used to fit equally well the D and the $2D$ line data. The value $\delta t_1 = 8.0$ eV is very high. However, one should notice that in Refs. 11 and 7 defects were induced in graphene by means of Ar^+ ion bombardment. This technique leads to the formation of carbon multivacancies in the sample. In Ref. 7, the defect average size is estimated, by means of scanning tunnel microscopy, to be 1.85 nm. On the contrary, the present model considers only point defects (the hopping parameters are changed by δt_1 for a single isolated carbon-carbon bond). The large value $\delta t_1 = 8.0$ eV is thus to be considered as an effective variation of the hopping parameter that mimics the existence of an extended defect (a realistic description of the defect should be done by considering the variation of the hopping parameters associated to many different neighboring sites). For less damaging defects, δt_1 will be smaller and the critical defect concentration, above which the D line intensity begins to decrease, will be larger than that of Fig. 17.

Finally, the behavior of the D line intensity as a function of the defect concentration has been discussed in literature using different models[7,11] (see also Ref. 42). To make a comparison, it can be useful to restate the present finding as follows. According to the DR perturbative model, the intensity of the defect-induced lines decreases by increasing the defect concentration when $\tilde{\gamma}^{(D)}$ becomes higher than $\tilde{\gamma}^{(ep)}$, that is, when the average length an electron/hole travels in between two scatterings events with a defect becomes smaller than the average length an electron/hole travels before scattering with an optical phonon.

D. Dependence of the spectra on the type of defect

Here, we discuss how the results depend on the type of defect. Calculations were done using three different model defects, namely hopping defects, on-site defects, and Coulomb ones (see Sec. II E for a description of the relevant parameters). Figure 18 compares calculations with the measurements from Ref. 11, which correspond to a defect concentration $n_d =$

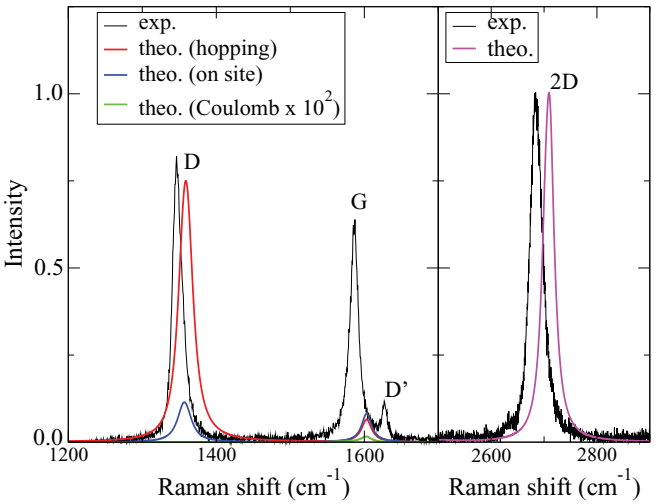

FIG. 18. (Color online) Calculated Raman spectra obtained for three different kinds of defects (hopping, on-site, and Coulomb), compared with the measurements of Ref. 11 done at $\epsilon_L = 2.4$ eV. The Raman G line is not described by the present model. Calculations are done using $\gamma^{\rm tot} = 96$ meV. Other relevant parameters are given in the text. All intensities are normalized by the corresponding $2D$ maximum. The intensity of the Coulomb impurity spectrum is enhanced by 10^2 for clarity.

10^{12} cm^{-2} and $\epsilon_L = 2.4$ eV. For the hopping and on-site defects, the calculations are done using $\alpha_{\rm hopp} = \alpha_{\rm on} = 6.4 \times 10^{13}$ eV^2 cm^{-2}, which, for the hopping defect, reproduces the ratio between the integrated areas of the measured D and $2D$ lines of Ref. 11. By choosing $\delta t_1 = \delta V_0 = 8.0$ eV (see also the discussion in Sec. III C 3), the above values of α correspond to a defect concentration $n_d = 10^{12}$ cm^{-2}. For Coulomb impurities, the distance between the impurity and graphene is $h = 0.27$ nm and $n_d = 10^{12}$ cm^{-2}.

From Fig. 18, the hopping defect is the best model to study defect-induced Raman processes. Indeed, contrary to the other models, the hopping defect provides a ratio of the intensities of the D and D' lines, which is in good agreement with measurements. The intensity ratio between D and D' strongly depends on the kind of model defect, suggesting that this ratio could possibly be used to experimentally determine the kind of defects present in a graphene sample. From Fig. 18, we also notice that Coulomb defects (charged impurities outside the graphene plane) provide an almost undetectable contribution to the Raman signal. Indeed, for a defect concentration of $n_d = 10^{12}$ cm^{-2}, the D line is absent and the D' intensity is almost three orders of magnitude smaller than the experimental one. We recall that Coulomb defects could be an important source of scattering during electronic transport in graphene (see Ref. 43 and references therein). The fact that they are not detectable by Raman spectroscopy (which is routinely used to characterize experimentally the quality of graphene samples) is thus a relevant issue, which deserves some more comments.

The present simulations consider a very short graphene/impurity distance h, in order to enhance the Raman signal of the Coulomb impurities. Indeed, $h = 0.27$ nm is the distance between K atoms and graphene planes in the KC_8 intercalated graphite. This distance corresponds to the experimental conditions of Ref. 43, where K^+ ions are

deposited on graphene. In the case, where the impurities are charges trapped in the substrate (e.g., SiO_2) a longer distance (e.g., 1 nm) is more appropriate. It is not surprising that the contribution of Coulomb impurities to the D line is completely negligible. Indeed, the Fourier transform of the Coulomb potential is maximum close to $\mathbf{\Gamma}$ and decays as $1/q$ far from it, Eq. (B10), and the D line is due to phonons near the $\mathbf{K}$ point and far from $\mathbf{\Gamma}$. This argument also suggests that the D' band, which is due to phonons near $\mathbf{\Gamma}$, should be more sensitive to the presence of Coulomb impurities. According to calculations, this is actually the case, however, for $\epsilon_L = 2.4$ eV and $n_d = 10^{12}$ cm^{-2} the ratio of the integrated area $A(D')/A(2D) = 1.5 \times 10^{-4}$, meaning that the presence of a D' band due to Coulomb impurities should not be detectable. The use of smaller energy laser increases the intensity of the D' signal since the excited phonons are nearer $\mathbf{\Gamma}$. However, for $\epsilon_L = 1.2$ eV and $n_d = 10^{12}$ cm^{-2}, $A(D')/A(2D) = 8.0 \times 10^{-4}$, which is still very small. Within the present model, $A(D')/A(2D)$ increases linearly by increasing the impurity concentration, n_d. n_d, however, cannot be higher than 10^{14} cm^{-2}, which corresponds to the density of K atoms in KC_8. On the other hand, for Coulomb impurity concentrations higher than 10^{12} cm^{-2} doping effects should become important. These should be associated to an increase of the electron-electron scattering contribution to the electronic broadening,[34] which, in turn, will prevent the D' intensity to become detectable. Concluding, the presence of charged impurities is not associated to a Raman D band. A D' band is present, but should not be easily detectable.

E. Interpretation of the results

This section is dedicated to the interpretation of the results. Section III E 1 describes which are the most important processes associated to the DR. Section III E 2 describes which are the phonon wave vectors contributing to each Raman band. Section III E 3 analyzes the dominant directions of the phonon wave vectors and Sec. III E 4 is dedicated to the interpretation of the small width of the main DR Raman lines.

1. Dominant processes and interference effects

In this section we analyze which are the dominant processes among those described in Fig. 1. We distinguish between two classes of processes: processes aa are those in which the two intermediate scattering processes are associated to both electron states or to both hole states (namely the processes $ee1$, $ee2$, $hh1$, and $hh2$, using the notation of Fig. 1); processes ab are those in which the two scattering processes are associated one to an electron state and the other to a hole state ($eh1$, $eh2$, $he1$, and $he2$ in Fig. 1). The distinction between aa and ab processes holds for both phonon-defect and two-phonon lines.

In general, for all the simulations performed here, the ab processes are, by far, dominant over the aa ones, that is, the largest part of the Raman intensities are due to ab processes. This is true for both phonon-defect and two-phonon lines. In general, among the ab processes, all the four processes $eh1$, $eh2$, $he1$, and $eh2$ are associated to intensities of the same order of magnitude. Indeed, Fig. 19 shows a typical Raman spectrum, in which we compare the actual spectrum $I_{\rm tot}$ with two spectra obtained by including only aa processes, I_{aa}, or ab ones, I_{ab}. More precisely, $I_{\rm tot}$ is the Raman intensity computed including all the processes; I_{aa} is computed by restricting the sums in α and β in Eqs. (3) only to the $ee1$, $ee2$, $hh1$, and $hh2$ processes; I_{ab} is computed by restricting the sums in α and β in Eqs. (3) only to the $eh1$, $eh2$, $he1$, and $he2$ processes. In general, $I_{\rm tot} \neq I_{aa} + I_{ab}$. From Fig. 19, $I_{ab} \gg I_{aa}$ for both the D and the $2D$ lines.

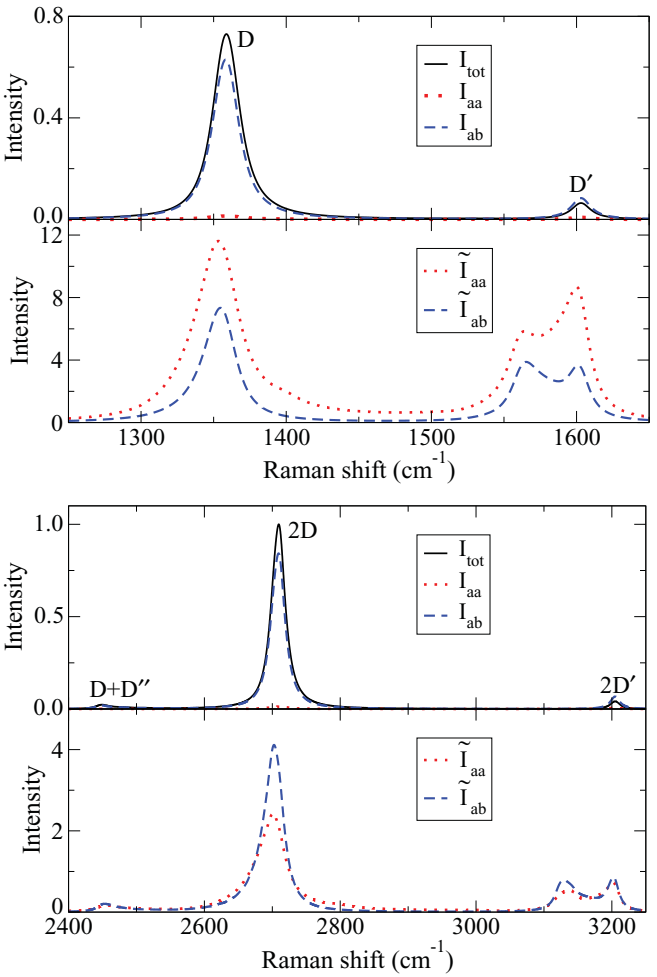

FIG. 19. (Color online) The upper panels compare the calculated Raman spectrum $I_{\rm tot}$ with spectra determined considering only aa processes, I_{aa}, or ab processes, I_{ab}. More precisely, $I_{\rm tot}$ is determined considering all the processes shown in Fig. 1; I_{aa} is computed by considering only $ee1$, $ee2$, $hh1$, and $hh2$ processes; I_{ab} is computed by considering only $eh1$, $eh2$, $he1$, and $he2$ processes (see the text). The lower panels display fictitious Raman intensities $\tilde{I}$ obtained by substituting to the DR scattering amplitudes K in Eqs. (3) their modulus $|K|$ (see the text). The two lines $\tilde{I}_{aa}$ and $\tilde{I}_{ab}$ are obtained by considering only aa and ab processes, as before. Calculations are done using $\epsilon_L = 2.4$ eV, $\gamma^{\rm tot} = 84$ meV, and hopping defects with $\alpha_{\rm hopp} = 6.4 \times 10^{13}$ eV^{2}cm^{-2}. All the intensities are normalized to the $2D$ line maximum of $I_{\rm tot}$.

The dominance of the ab processes is due to quantum interference effects. In particular, from Eq. (3), the Raman intensity for a given $\mathbf{q}$ results from a sum over $\mathbf{k}$ of $K(\mathbf{k})$ scattering amplitudes, which are complex numbers. The sum of these complex numbers can interfere in a constructive way, as for the ab processes, or in a destructive way, as for the aa processes. In particular, the DR condition determines

that for some resonant electronic wave vectors $\mathbf{k}_r$, $|K(\mathbf{k}_r)|$ should have a maximum. This maximum can be enhanced or suppressed by the interference of $K(\mathbf{k}_r)$ with the $K(\mathbf{k})$ at wave vectors $\mathbf{k}$, which are not exactly at the resonance (this point is further discussed in Appendix D). It is important to remark that, according to the present calculations, the DR scattering amplitudes K are complex numbers in which the real and imaginary parts are of the same order of magnitude even for the $\mathbf{k} = \mathbf{k_r}$ wave vectors that satisfy the DR condition.

To quantify the importance of quantum interference, we consider a fictitious Raman intensity $\tilde{I}$, which is obtained by substituting their modulus $|K|$ to the scattering amplitudes K in Eqs. (3). As example, in Eqs. (3) we substitute $I_{\mathbf{q}}^{pp} = |\sum_{\mathbf{k},\beta} K_\beta(\mathbf{k},\mathbf{q})|^2/N_k$, with $\tilde{I}_{\mathbf{q}}^{pp} = |\sum_{\mathbf{k},\beta} |K_\beta(\mathbf{k},\mathbf{q})||^2/N_k$.

Thus within the intensities $\tilde{I}$, the presence of possible destructive interference effect is canceled. Figure 19 shows a typical $\tilde{I}$ spectrum, in which we compare $\tilde{I}_{aa}$ and $\tilde{I}_{ab}$ obtained by solely including aa or ab processes. The ratio $\tilde{I}_{ab}/\tilde{I}_{aa}$ is very different from I_{ab}/I_{aa} for both the D and the $2D$ lines. In particular, $\tilde{I}_{ab}$ is no more dominant and it is always comparable in intensity to $\tilde{I}_{aa}$. Thus the fact that $I_{ab} \gg I_{aa}$ is indeed due to destructive interference effects. Moreover, certain lines of the fictitious $\tilde{I}$ spectrum, such as the D' or the $2D'$, do not appear as narrow and well defined lines as they are in the actual Raman spectrum I. Thus interference effects also play a role in determining the shape of certain lines.

Notice that, often, when discussing the DR processes, it is used a simplified argument, which consists in finding the electronic and phonon states which let two (or more) of the denominators in Eq. (1) go to zero. The assumption is that the physics is led only by those scattering amplitudes K that satisfy the DR condition. This simplified approach, which we call the "resonance argument," has been extensively used in literature with success (e.g., to determine the momenta of the phonons associated to certain lines), despite the fact that, within this approach, the possible role of quantum interference is completely neglected. The results of the previous paragraph show that in certain specific situation the "resonance argument" can be very misleading. For example, on the basis of a "resonance argument" one would deduce that the intensity associated aa processes are of the same order of magnitude as that associated to the ab ones (indeed, $\tilde{I}_{aa} \sim \tilde{I}_{ab}$ in Fig. 19), which is not the case.

We remark that several authors describe the DR by simply considering the aa processes (usually the ee processes in Figs. 1 and 4), as it is done in the seminal work by Thomsen and Reich.[10] However, following the present conclusions, these processes cannot be used alone to describe quantitatively the intensities of the D and $2D$ lines. The importance of interference effects in determining the shape of the DR Raman lines has been already outlined by Maultzsh *et al.* in Ref. 29. However, Ref. 29 just considers ee processes and completely neglects the ab ones, which are the most important. The fact the ab processes should be dominant for the $2D$ line has been argued by Basko in Ref. 23. But this conclusion is reached on the basis of a "resonance argument." Indeed, according to Ref. 23, the ab processes should be dominant because within these processes one can reach a condition in which all the transitions are real (nonvirtual) and the three denominators of Eq. (1) can be nullified simultaneously (triple resonance). As already said, this kind of argument cannot be applied to describe the intensity of the $2D$ line (basically, the conclusion is good but the argument is wrong). The best way to understand this point is to put to zero the phonon energies $\hbar\omega_{\mathrm{ph}}$ in all the denominators of the Raman scattering amplitudes K [e.g., in Eqs. (4) and (5)]. By doing this, the triple resonance condition of Basko applies also to the aa processes (not only to the ab). However, actual calculations show that I_{ab} remains much larger than I_{aa} even when $\hbar\omega_{\mathrm{ph}} = 0$. Actually, the intensity and the shape of the $2D$ line are marginally affected by including or not including $\hbar\omega_{\mathrm{ph}}$ in the denominators of the Ks (see Fig. 27 in Appendix C). We also remark that the triple resonance argument does not explain why $I_{ab} \gg I_{aa}$ also for the D line. Finally, Ref. 44 argues that quantum interference *in real space* plays a crucial role in enhancing the role of the ab processes versus the aa ones, for the D line. However, the model of Ref. 44 predicts a behavior that is in contrast with the present calculations.[45] Notice that the model of Ref. 44 was developed to describe extended defects such as edges, while here we are considering point defects.

The main conclusion of this section is that the ab processes ($eh1$, $eh2$, $he1$, and $eh2$ processes of Figs. 1 and 4) are responsible for most of the Raman intensity because of quantum interference. We remark that this conclusion is not due to the complex details of the present calculations but can be deduced with a very simplified model in which the scattering matrix elements in the numerator of Eq. (1) are constant, the phonon energies in the denominators [e.g., $\hbar\omega_{\mathbf{q}}^{\nu}$ in Eqs. (4) and (5) are neglected, and in which the electronic bands are conic. This simple model can also be used to shed light on the role played by quantum interference; see Appendix D.

2. *Phonons wave vectors associated to the Raman lines*

We now discuss which phonons are responsible for the lines presented in Figs. 6 and 7. In Fig. 20, we consider the most important Raman lines and we decompose the Raman intensity of a given band into its components associated to phonons with a given wave vector $\mathbf{q}$. For the defect-induced bands, D, D', and D'', we plot $\mathcal{I}_{\mathbf{q}} = \sum_{\nu}^{*} I_{\mathbf{q}\nu}^{\mathrm{pd}}$, and for the two-phonon bands, $2D$, $2D'$, and $D + D''$, we plot $\mathcal{I}_{\mathbf{q}} = \sum_{\nu,\mu}^{*} I_{\mathbf{q}\nu\mu}^{pp}$, with $I_{\mathbf{q}\nu}^{\mathrm{pd}}$ and $I_{\mathbf{q}\nu\mu}^{pp}$ defined in Eq. (3) and the symbol * indicates that the summation is restricted to a frequency window corresponding to a given Raman band (see Ref. 46). The $\mathbf{q}$-dependent intensity $\mathcal{I}_{\mathbf{q}}$ discloses which are the phonon wave vectors $\mathbf{q}$ that mostly contribute to a given Raman line. The most remarkable result from Fig. 20 is that these phonons belong to limited regions of the BZ consisting in very narrow (almost one-dimensional) lines. As expected, the D, D'', $2D$, and $D + D''$ Raman bands originate from phonon $\mathbf{q}$ wave vectors belonging to a closed line around the $\mathbf{K}$ and $\mathbf{K'}$ high-symmetry points.

In literature, the DR condition on the virtual transitions is often used to determine the Raman-dominant phonon wave vectors (see, e.g., Refs. 10, 47, 14, 48, 1, and 9). To verify the validity of such a procedure, we focus on the $2D$ line, which is mostly due to eh processes (Sec. III E 1) and consider an excitation energy $\epsilon_L = 2.4$ eV. The DR consists in three processes of excitation, phonon scattering, and recombination. The $\mathbf{k}$ vectors of the electronic states, which are excited by a laser with energy ϵ_L, form a triangularly distorted closed line, as the isoenergy contour surrounding the $\mathbf{K}$ point in Fig. 21(a).

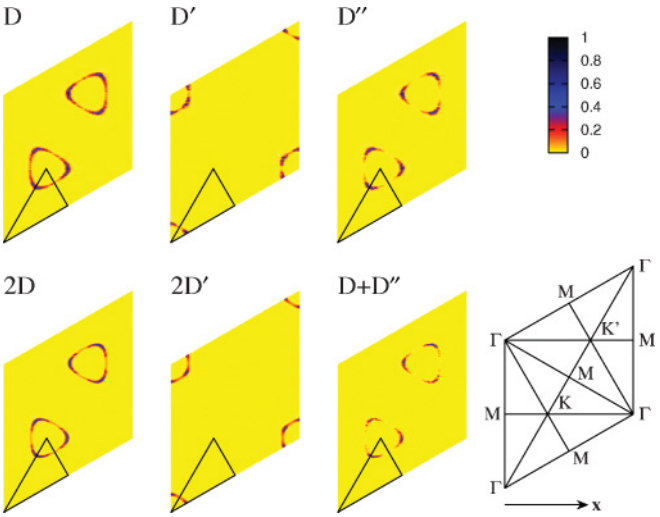

FIG. 20. (Color online) Decomposition the intensity of the most important Raman bands into their components associated to phonons with a given wave vector $\mathbf{q}$, $\mathcal{I}_{\mathbf{q}}$. The rhombi are the graphene first Brillouin zone. For each band, we consider the contribution to the Raman intensity in a window of frequencies corresponding to that particular band (Ref. 46). The intensities are normalized to the maximum of each band. Calculations are done using $\epsilon_L = 2.4$ eV, $\gamma^{\text{tot}} = 84$ meV, and hopping defects with $\alpha_{\text{hopp}} = 6.4 \times 10^{13}$ eV^2 cm^{-2}.

The states involved in the emission of a quantum of light with energy $\epsilon_L - 2\hbar\omega^{\nu}_{\mathbf{q}}$ (recombination) form a second triangularly distorted closed line, as the isoenergy contour surrounding the $\mathbf{K}'$ point in Fig. 21(a). These isoenergy contours are expected to give the important contribution to the DR, although the energy is not conserved in the intermediate virtual transitions. The intermediate DR processes are associated to a phonon $\mathbf{q}$ and the important processes are expected to be those associated to $\mathbf{q}$ vectors that connect the two triangles of Fig. 21(a). In particular, let us translate the $\mathbf{K}$ triangle by $\mathbf{q}$ and let us consider the nesting vectors ($\mathbf{q}_n$) for which the $\mathbf{K}$ triangle becomes tangent to the $\mathbf{K}'$ one, as in Fig. 21(b). These phonon wave vectors are expected to dominate the Raman spectra, since for such nesting vectors there is a high density of electronic transitions satisfying the DR mechanism.[14,48] The $\mathbf{q}_n$ vectors are shown in Fig. 21(c) as a dashed white line, which is compared with the Raman intensity $\mathcal{I}_{\mathbf{q}}$ from our most precise calculation (as in Fig. 20). Within the scale of the figure, the nesting vectors reproduce very well the maximum of the $\mathcal{I}_{\mathbf{q}}$, meaning that the simple picture of Fig. 21(b) provides a quantitative prediction of the relevant phonon momenta.

To generalize the analysis to an arbitrary laser excitation energy, we now consider the isoenergy electronic contours as those of Fig. 21(a) for different values of ϵ_L. For each ϵ_L, we determined the phonon $\mathbf{q}_n$ vectors that are nesting the corresponding contours. Among these points, we consider only the vectors along high-symmetry lines. In this case the nesting vectors, $\mathbf{q}_{\text{inner}}$ and $\mathbf{q}_{\text{outer}}$, can be easily extracted from the one-dimensional electronic-band dispersion along the high-symmetry line, as schematically shown in Fig. 22. In the lower panel of Fig. 23 we report $\mathbf{q}_{\text{inner}}$ and $\mathbf{q}_{\text{outer}}$ obtained by the DR condition of Fig. 22 as a function of ϵ_L. In Fig. 23, we also report the corresponding vectors obtained by finding the maximum intensity in the $\mathcal{I}_{\mathbf{q}}$ plots (as those in Fig. 20)

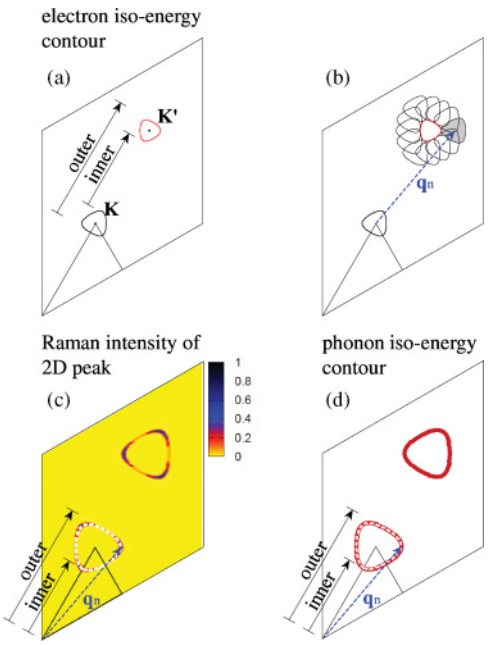

FIG. 21. (Color online) Electron and phonon states relevant for the $2D$ line. The rhombi are the graphene Brillouin zone. (a) The triangularly distorted contour around $\mathbf{K}$ is obtained from $\epsilon^{\pi^*}_{\mathbf{k}} - \epsilon^{\pi}_{\mathbf{k}} = 2.4$ eV and represents the electronic states near $\mathbf{K}$ that are excited by a laser with energy $\epsilon_L = 2.4$ eV. The contour around $\mathbf{K}' = 2\mathbf{K}$ is obtained from $\epsilon^{\pi^*}_{\mathbf{k}} - \epsilon^{\pi}_{\mathbf{k}} = 2.06$ eV and represents the electronic states near $\mathbf{K}'$ that are deexcited by the emission of a quantum of light with energy $\epsilon_L - 2\omega_{\text{ph}}$ eV, with $\omega_{\text{ph}} = 1354$ cm^{-1} (half the energy of the $2D$ line for $\epsilon_L = 2.4$ eV). (b) $\mathbf{q}_n$ is one of the vectors such that the contour near $\mathbf{K}$ translated by $\mathbf{q}_n$ is tangent to the contour near $\mathbf{K}'$. (c) $\mathcal{I}_{\mathbf{q}}$ decomposition of the $2D$ intensity (same figure as the $2D$ panel in Fig. 20). The dashed closed line is defined by the ensemble of the $\mathbf{q}_n$ vectors. (d) The dashed line is the same as in (c). The thick gray (red) line is the phonon isoenergy contour obtained from $\omega^{\nu}_{\mathbf{q}} = 1354$ cm^{-1}. The relevant phonon branch, thick gray line in Fig. 4, is disentangled from the other branches as in Fig. 2 of Ref. 28. Notice that the isoenergy contours of electron states [panels (a) and (b)] and phonons [panels (c) and (d)] have opposite trigonal warpings. Notice also that phonon isoenergy contours in Fig. 2 of Ref. 28 are plotted with respect to the $\mathbf{K}'$ of the present notation.

corresponding to that excitation energy. The sets of $\mathbf{q}$ vectors obtained with these two different procedures nicely coincide.

We remark that the simplified scheme of Figs. 21(b) and 22 is used for the $2D$ line, and that its validity comes *a posteriori* after the comparison with our most precise calculations. The analogous construction for the $2D'$ line works equally well, as can be seen in Fig. 24(b), by comparing the nesting vector profile (dashed line) with the $\mathcal{I}_{\mathbf{q}}$ decomposition of the $2D'$ intensity.

3. *Dominant directions of the Raman phonon wave vectors*

A close look at Fig. 20 reveals that the most intense contributions of D, D'', $2D$, and $D + D''$ are due to $\mathbf{q}$ points along the high-symmetry directions $\mathbf{K} \rightarrow \mathbf{\Gamma}$ and $\mathbf{K}' \rightarrow \mathbf{\Gamma}$. The D' and $2D'$ bands originate from a closed line around $\mathbf{\Gamma}$ and the most intense contributions are due to $\mathbf{q}$ points along the high-symmetry $\mathbf{\Gamma} \rightarrow \mathbf{M}$ direction.

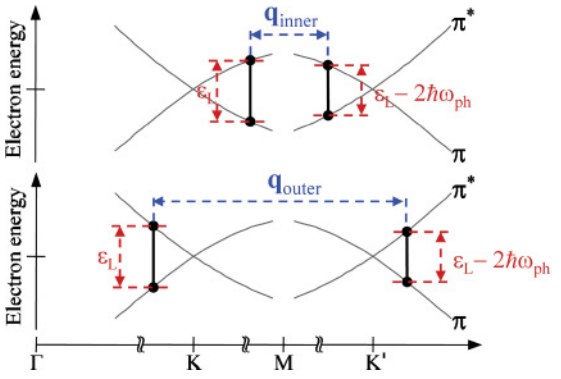

FIG. 22. (Color online) Scheme of the double-resonant process associated to the $2D$ line. The momenta of the phonons mostly involved are indicated as "inner" and "outer."

To analyze the results we consider the following definitions. The intensities $\mathcal{I}_{\mathbf{q}}$ (Fig. 20) form, basically, a closed profile surrounding one high-symmetry point (**K** for the D and $2D$ lines, and **Γ** for the $2D'$). Taking the high-symmetry point as the reference, we consider how the intensity of a given Raman band varies as a function of the direction $\hat{q}$ of the vector **q**. Thus in the lower panel of Fig. 25 we plot $\mathcal{I}_{\hat{q}} = \int_0^{\bar{q}} q dq \mathcal{I}_{\mathbf{q}}$, where the integral is done in a region containing the most intense contribution. It is also interesting to consider the intensity weighted average phonon frequency associated to a given Raman band and to a given **q** point, $\langle\omega_{\mathbf{q}}\rangle$. As an example, for the two-phonon lines $\langle\omega_{\mathbf{q}}\rangle = [\sum^*_{\nu,\mu} I^{pp}_{\mathbf{q}\nu\mu}(\omega^{\nu}_{\mathbf{q}} + \omega^{\mu}_{\mathbf{q}})]/[\sum^*_{\nu,\mu} I^{pp}_{\mathbf{q}\nu\mu}]$, where the summation is restricted to the corresponding frequency window.[46] This quantity, basically, gives the frequency of the phonons associated to that Raman band. In analogy to $\mathcal{I}_{\hat{q}}$, we define $\langle\omega_{\hat{q}}\rangle$ as the average of $\langle\omega_{\mathbf{q}}\rangle$ along a direction $\hat{q}$ of the vector **q**. Here, also, the origin of $\hat{q}$ is **K** for the D and $2D$ lines, and **Γ** for the $2D'$. Figure 25 shows the angular dependence of the averaged phonon frequency $\langle\omega_{\hat{q}}\rangle$ for the D, $2D$, and $2D'$ lines (actually, the shifts in the upper panel of Fig. 25 are obtained after an average on a small-angle interval from $\theta - \Delta\theta$ to $\theta + \Delta\theta$).

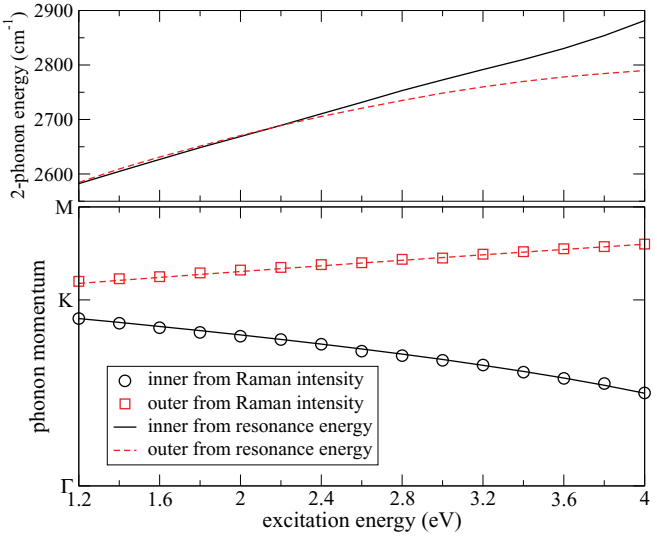

FIG. 23. (Color online) Lower panel: momenta of the inner and outer high-symmetry phonons which mostly contribute to the $2D$ band. The lines are obtained from the vectors connecting the isoenergy electronic contours corresponding to that excitation energy. For example, the values for $\epsilon_L = 2.4$ eV are the moduli of the inner and outer vectors reported in Figs. 21 and 22. The symbols are obtained from the maximum intensity in the $\mathcal{I}_{\mathbf{q}}$ plots (as those in Fig. 20 or in the left panels of Fig. 26) corresponding to that excitation energy. Upper panel: frequency of the inner and outer phonons reported in the lower panel.

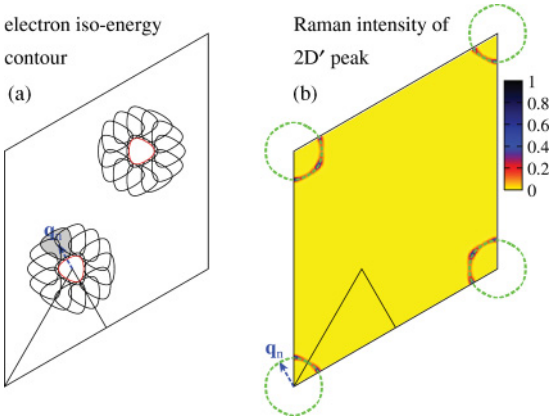

FIG. 24. (Color online) Electron and phonon states relevant for the $2D'$ line. (a) The triangularly distorted contours around **K** are obtained from $\epsilon^{\pi^*}_{\mathbf{k}} - \epsilon^{\pi}_{\mathbf{k}} = 2.4$ eV and $\epsilon^{\pi^*}_{\mathbf{k}} - \epsilon^{\pi}_{\mathbf{k}} = 2.0$ eV. They represent the electronic states that are excited by a laser with energy $\epsilon_L = 2.4$ eV and those that are deexcited by the emission of a quantum of light with energy $\epsilon_L - 2\omega_{\text{ph}}$ eV, with $\omega_{\text{ph}} = 1602$ cm^{-1} (half the energy of the $2D'$ line for $\epsilon_L = 2.4$ eV). $\mathbf{q}_n$ is one of the vectors such that the excited-states' contour translated by $\mathbf{q}_n$ is tangent to the second contour. The analogous construction arond **K**′ is also shown. (b) $\mathcal{I}_{\mathbf{q}}$ decomposition of the $2D'$ intensity (same figure as the $2D'$ panel in Fig. 20). The two dashed (green) closed lines (almost indistinguishable in the scale of the figure) are defined by the ensemble of the nesting $\mathbf{q}_n$ vectors among **K** states or among **K**′ states.

Let us consider the D and $2D$ bands. From Fig. 25, the phonons along the $\mathbf{K} \rightarrow \mathbf{\Gamma}$ directions (in literature these are usually called "inner" phonons; Fig. 22) provide a contribution that is almost four times higher than the one from the $\mathbf{K} \rightarrow \mathbf{M}$ ones ("outer" phonons). Contrary to the present findings, in literature it is usually assumed[1,10,14] that the phonons which mostly contribute to the D and $2D$ lines are outer phonons (along $\mathbf{K} \rightarrow \mathbf{M}$). Only very recently some authors have outlined the possible importance of the inner phonons ($\mathbf{K} \rightarrow \mathbf{\Gamma}$).[18–22] The present finding is counterintuitive and stems from the complex behavior of the scattering matrix elements in the numerators of Eq. (1). To understand this point, in Fig. 25 we show the results of calculations in which the numerators in Eq. (1) are taken as a constant [that is, independent form **k** and **q** as, e.g., in Eqs. (4) and (5). Within this simplified approach (which completely neglects, for example, the dependence electron-phonon scattering matrix elements on **q**) the outer phonons become dominant (in Fig. 25, lower panel, the intensity has the maximum along the $\mathbf{K} \rightarrow \mathbf{M}$ direction for both D and $2D$), in agreement with the simplified models previously used in literature, but in disagreement with our most precise calculations. Concluding, inner processes are dominant for both D and $2D$ lines. A proper description of

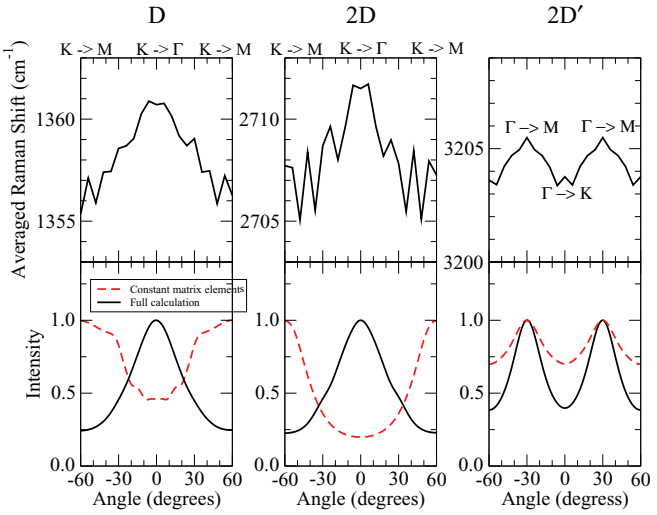

FIG. 25. (Color online) Angular dependence of the intensity (lower panels) and of the weighted average Raman shift (upper panels) for the D, $2D$, and $2D'$ bands. The angles are measured taking the horizontal direction in Fig. 20 as reference. Thus for the D and $2D$ bands, 0° is the $\mathbf{K} \rightarrow \mathbf{\Gamma}$ direction in the BZ, while ±60° are the $\mathbf{K} \rightarrow \mathbf{M}$ one. For the $2D'$ band, zero degrees is the $\mathbf{\Gamma} \rightarrow \mathbf{K}$ direction, while, ±30° are the $\mathbf{\Gamma} \rightarrow \mathbf{M}$ direction. In the lower panels, the solid lines correspond to our most precise calculation. Dashed lines correspond to an approximated simulations in which the electron-light, electron-phonon, and electron-defect scattering matrix elements are kept constant (see the text). Calculations are done using $\epsilon_L = 2.4$ eV, $\gamma^{\text{tot}} = 84$ meV, and hopping defects with $\alpha_{\text{hopp}} = 6.4 \times 10^{13}$ eV^2 cm^{-2}.

the electronic scattering matrix elements (in particular of the electron-phonon coupling) is crucial to obtain this result.

4. Width of the Raman bands

One of the most interesting features of the simulated Raman spectra of Figs. 6 and 7 is the narrow width of the bands, which reproduces the measured spectra. The narrow width of the D and $2D$ lines is indeed surprising since already at $\epsilon_L = 2.4$ eV the electronic states involved in the Raman process display an important trigonal warping [i.e., the electron isoenergy contours are triangularly distorted as in Fig. 21(a)]. In the presence of trigonal warping one should expect the excited phonons to have energies distributed in a broad range. Indeed, previous calculations[14,17] did not reproduce narrow line shape of the DR lines. The present improved description of the electronic scattering matrix elements partially explains such narrow lines. The most important role is played by the phonon energy dispersions. The upper panels of Fig. 25 show that, for the D, $2D$, and $2D'$ lines at $\epsilon_L = 2.4$ eV, the excited phonons have almost the same energy (within ∼5 cm^{-1}), despite the strong electron trigonal warping. This fact explains the small width of the DR Raman lines and it is due to the details of the phonon dispersion we used. Indeed, with a reasonable description of the electronic trigonal warping and using a rough description of the phonon energies, larger dispersions in frequencies (and broader Raman lines) are found.[17] Reference 28 has clearly demonstrated that the phonon trigonal warping is important and that it is opposite to the electronic one. The present results show that, as already argued in Ref. 28, the interplay between the electronic and phononic trigonal warping provides a sort of cancellation. This results in the small dispersion of the phonon frequencies of the upper panel of Fig. 25 and, consequently, in the small width of the associated Raman lines.

To illustrate the concept of trigonal warpings cancellation, Fig. 21(d) compares the line of the nesting vectors $\mathbf{q}_n$ [white dashed line; see Fig. 21(b) and Sec. III E 2] with the isoenergy contour of the phonons having half the energy of the $2D$ (thick red lines). The two lines nicely resemble each other, meaning that all the nesting phonons have nearly the same energy and, as a consequence, the $2D$ linewidth is small. If the phonon isoenergy contour was different, the two lines would not superimpose and the $2D$ line would have a broader shape. The perfect cancellation of electronic and phononic trigonal warping breaks down for laser energy in the UV range. Indeed in the upper panel of Fig. 23, we report, as a function of ϵ_L, the frequency associated with the inner and outer phonons. At $\epsilon_L = 2.4$ eV, the frequencies associated to inner and outer phonons almost coincide. However, for higher ϵ_L, the two frequencies become different, meaning that for a sufficiently high ϵ_L the $2D$ line is expected to become broader.

Indeed, according to our most precise calculations, at $\epsilon_L = 3.8$ eV the Raman $2D$ band appears much broader than the one at $\epsilon_L = 2.4$ eV and displays two maxima at 2790 and 2840 cm^{-1} (Fig. 8). At $\epsilon_L = 3.8$ eV (Fig. 26) the angular dependence of the average frequency shift is more dispersive than in the $\epsilon_L = 2.4$ eV case. The inner phonons correspond to the highest frequency components, $2D^+$ at ∼2840 cm^{-1}, and the outer phonons to the lowest one, $2D^-$ at ∼2790 cm^{-1}. In Fig. 26 we also show the $\mathbf{q}$ vectors' decomposition of the intensities of the $2D^+$ and $2D^-$ components. For the $2D^+$, the shape is triangularly distorted and the maximum corresponds to the inner phonons, while for the $2D^-$ the maximum corresponds to the outer phonons.

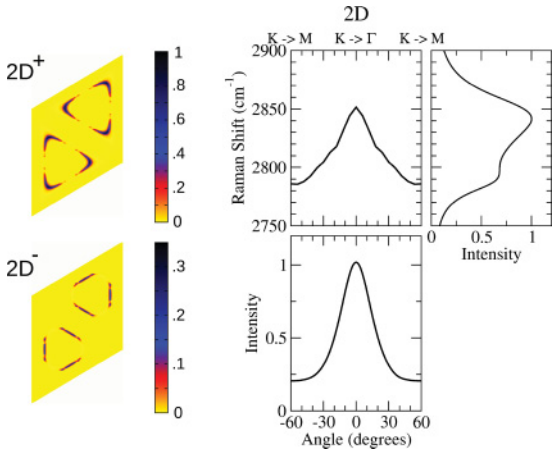

FIG. 26. (Color online) Calculated $2D$ line for the excitation $\epsilon_L = 3.8$ eV and $\gamma^{\text{tot}} = 170$ meV. Top right panel: intensity vs Raman shift. The line appears as a broad band with two maxima near 2790 cm^{-1} ($2D^-$) and 2840 cm^{-1} ($2D^+$). Left panels: mapping of the Raman intensity in the Brillouin zone (as in Fig. 20) of the two components $2D^-$ $2D^+$ obtained by integrating in the corresponding frequency windows (Ref. 46). Central panels: angular dependence of the weighted average Raman shift and of the intensity, as in Fig. 25

IV. CONCLUSIONS

We calculated the double-resonant Raman spectrum of graphene with a computational method, which tries to overcome the most common approximations used in literature. Calculations are done using the standard approach based on the golden rule generalized to the fourth perturbative order[10] [Eq. (1)]. We determined the Raman lines associated to both phonon-defect processes (defect-induced excitations of $\mathbf{q} \neq \mathbf{0}$ phonons, such as in the D, D', and D'' Raman lines) and two-phonon processes (excitations in a defect-free sample of a $-\mathbf{q}$ and a $\mathbf{q}$ phonons, such as in the $2D$, $2D'$, or $D + D''$ lines). The lowest-order processes (excitation of a $\mathbf{q}= 0$ phonon, such as in the G line) and higher-order processes (such as in the $D + D'$ line at $\sim$2900 cm^{-1}, which is usually attributed to a defect-induced excitation of two phonons $\mathbf{q}$ and $\mathbf{q}'$ with $\mathbf{q} + \mathbf{q}' \neq \mathbf{0}$) are not described by the present approach.

The electronic summation is performed all over the two-dimensional Brillouin zone and all the possible phonons (with any wave vector) are considered. Electronic bands are obtained from a five-neighbor tight-binding (TB) approach in which the parameters are fitted to reproduce *ab initio* calculations based on density-functional theory (DFT) corrected with GW. This procedure provides a Fermi velocity (the slope of the Dirac cone) in good agreement with measurements and a good description of the trigonal warping. The resulting electron/hole asymmetry is not negligible. The phonon dispersion is obtained from fully *ab initio* DFT calculations corrected with GW. This procedure is necessary to obtain a good description of the slope of the phonon branch associated with the D and $2D$ lines, near $\mathbf{K}$. The electron-phonon, electron-light, and electron-defect scattering matrix elements are obtained within the TB approach. The defect-induced Raman processes are simulated by considering three different kinds of model defects: (i) *on-site defects*, obtained by changing the on-site TB parameter; (ii) *hopping defects*, obtained by changing one of the first-neighbor hopping TB parameters; (iii) *Coulomb defects*, corresponding to charged impurities adsorbed at a given distance from the graphene sheet, which interact with graphene through a Coulomb potential.

The electronic linewidth (the inverse of the electronic lifetime), which turns out to be a very relevant parameter, is calculated explicitly considering the contributions from electron-phonon and electron-impurity scattering. To give an idea, for $\epsilon_L = 2.4$ eV, in the absence of defects and for zero doping, the sum of the electron and hole linewidths is $\gamma^{\text{tot}} = 84$ meV (which is roughly two times the full width at half maximum of the electron spectral function).

By looking at the overall shape of the typical Raman spectra, for an excitation energy of $\epsilon_L = 2.4$ eV, the agreement between calculations and measurements is very good. In particular, all the Raman lines observed experimentally, even the small intensity ones, are present in the calculated spectra and the relative intensities among two-phonon lines (such as $2D$, $2D'$, or $D + D''$ lines) or among phonon-defect lines (such as the D and the D' lines) are correctly reproduced (with the hopping defect being the best model to study defect-induced Raman processes). The most remarkable agreement between theory and measurements relates to the linewidths. Indeed, the present calculations reproduce very well the measured small widths of the D, D', $2D$, and $2D'$ lines. Moreover, calculations reproduce quite well the symmetric Lorentzian shapes of the $2D$ and $2D'$ lines and the asymmetric shape of $D + D''$ band. We remark that, in the present model, the only parameter used to fit Raman measurements, α_{hopp}, determines the ratio of the D versus $2D$ intensities but does not affect the relative intensities among phonon-defect or two-phonon lines, the width of the lines, and their shape.

We determined how the Raman spectra change by changing the laser excitation energy ϵ_L from 1.2 to 4.0 eV, which are the energies mainly used experimentally. All the visible lines change in position, intensity, and shape. In particular, the $2D$ line has a small-width Lorentzian shape for $\epsilon_L \leqslant 2.4$ eV and it is asymmetric and broader at $\epsilon_L = 3.8$ eV. The measured shift of the Raman line position as a function of ϵ_L is well reproduced for all the available measurements. The calculated spectra also display some small intensity bands associated to acoustic phonons. Some of them, such as the $D' + D^3$ and the $D' + D^4$ (in the 1800–2000-cm^{-1} range) are actually visible in the measured spectra.[36,37] Finally, for high-energy excitations, e.g., $\epsilon_L = 3.8$ eV, the most intense Raman lines ($2D$ and D) change shape and intensity as a function of the polarization of the light. This finding is remarkable since it could lead to measurable effects.

We determined how the intensity of the main DR Raman lines is affected by various parameters such as the electronic linewidth, the excitation energy, and the defect concentration. The absolute intensity of the double-resonant Raman lines is strongly affected by the actual value of the electronic linewidth γ^{tot}. In general, the intensity of a DR Raman line decreases when the electronic linewidth increases (at fixed defect concentration) because the electronic broadening tends to kill the double-resonance condition. According to the present findings, also the ratio of the intensities of the $2D$ and $2D'$ lines depends on γ^{tot}. This result is particularly appealing since the measurement of this ratio (followed by the comparison with the present calculations) could be used to determine experimentally the electron/hole linewidth γ^{tot} and, in particular, its components due to defects and/or to electron-electron scattering in doped samples. We determined how the intensity ratio among various Raman lines change as a function of the excitation energy of the laser. In particular, we determined the evolution of $A(2D')/A(2D)$, $A(D + D'')/A(2D)$, $A(D'')/A(D)$, and $A(D')/A(D)$ [where $A(X)$ is the integrated area under the X Raman line] as a function of the excitation energy. All these ratios considerably change in the range of excitation energies available experimentally, however, measurements to compare with are not presently available.

We studied the dependence of the D and $2D$ lines' intensity on the defect concentration, comparing to recent measurements.[7,11] We first remind that the electronic linewidth γ^{tot} is given by the sum of an intrinsic component $\tilde{\gamma}^{(ep)}$ (due to the electron-phonon interaction) and an extrinsic defect-induced component $\tilde{\gamma}^{(D)}$, which increases linearly by increasing the defect concentration. The intensity of the $2D$ line monotonously decreases by increasing the defect concentration n_d. Indeed, the $2D$ line (which is a two-phonon process) depends on n_d only through the electronic linewidth γ^{tot}, which, in turn, increases by increasing n_d. The intensity of the D line has a nonmonotonic behavior. The D line (which is a defect-induced process) depends on n_d through two distinct

mechanisms: first there is a proportionality factor between the Raman intensity and n_d; second, the linewidth $\gamma^{\rm tot}$ depends on n_d as for the $2D$ line. For small n_d, $\gamma^{\rm tot} \sim \tilde{\gamma}^{(ep)}$ and the D intensity increases linearly with n_d. For high n_d, the dependence of $\gamma^{\rm tot}$ on n_d becomes the dominant mechanism, leading to a decrease of the intensity, as for the $2D$ line. The maximum of the D intensity is reached for the defect concentration corresponding to the condition $\tilde{\gamma}^{(D)} \sim \tilde{\gamma}^{(ep)}$.

We have compared Raman spectra calculated with the three different model defects. The intensity ratio between the defect-induced D and D' lines strongly depends on the kind of model defect, suggesting that this ratio could possibly be tuned in actual experiments by selecting a special kind of impurities on the sample. Charged impurities outside the graphene plane (Coulomb defects) could be an important source of scattering during electronic transport. However, according to the present calculations, they should provide an almost undetectable contribution to the Raman signal, the D line being completely absent and the D' having an intensity orders of magnitude smaller than the $2D$ line.

Finally, the analysis of the results has focused on certain specific issues currently debated.

Among the different possible DR processes, the electron-hole ones (processes in which both electronic and hole states are involved in the scattering, *ab* in the text) are responsible for most of the Raman intensity of both the D and the $2D$ lines. Several authors (e.g., Ref. 10) describe the DR by simply considering electron-electron or hole-hole processes (processes in which only electrons or only holes are involved in the scattering, *aa* in the text) which, according to the present findings, give a negligible contribution to the Raman intensity. The dominance of the electron-hole processes stems from the presence of a destructive quantum interference that kills the contribution of the electron-electron and hole-hole ones. This conclusion is not due to the complex details of the present calculations but can be deduced with a very simplified model, easy to implement.

The most intense contribution to both the D and $2D$ lines is due to phonons along the high-symmetry directions $\mathbf{K}\rightarrow\mathbf{\Gamma}$ (*inner* phonons). This is contrary to the common assumption[1,10,14] that the phonons that mostly contribute to the D and $2D$ lines belong to the $\mathbf{K}\rightarrow\mathbf{M}$ direction (*outer* phonons). The present result (the dominance of the inner phonons) is counterintuitive and stems from the complex behavior of the electronic scattering matrix elements in the numerator of the double-resonance scattering amplitude.

The observed small width of the $2D$ line at $\epsilon_L = 2.4$ eV is explained as a consequence of the interplay between the opposite trigonal warpings of the electron and phonon dispersions: the excited electronic states form a triangularly distorted profile having vertex along the $\mathbf{K}\rightarrow\mathbf{M}$ direction, while the phonon isoenergy contour is a triangularly distorted profile having a vertex along the $\mathbf{K}\rightarrow\mathbf{\Gamma}$ direction. Because of this, the excited phonons (both the inner and the outer ones) have almost the same energy and, as a consequence, the $2D$ linewidth is small. At higher excitation energies this condition is no more verified and the $2D$ line becomes broader and asymmetric. For instance, at $\epsilon_L = 3.8$ eV the calculated spectrum displays two maxima corresponding to a main component at $\sim$2840 cm^{-1} (due to inner phonons) and to a less intense one at $\sim$2790 cm^{-1} (due to outer phonons).

ACKNOWLEDGMENTS

We thank D. Basko and P. Gava for usefull discussions. P.V. has received financial support from the Conselho Nacional de Desenvolvimento Científico e Tecnológico (CNPq), Brazil. Part of the calculations were performed at IDRIS (France), Project No. 096128.

APPENDIX A: RAMAN DOUBLE-RESONANT SCATTERING AMPLITUDES

Explicit expressions are now given for all the double-resonant scattering amplitudes $K^{\rm pd}(\mathbf{k},\mathbf{q},\nu)$ and $K^{pp}(\mathbf{k},\mathbf{q},\nu,\mu)$, which have been included in the sums of Eq. (3). The following processes are described diagrammatically in Fig. 1. The arguments $\mathbf{k}$, $\mathbf{q}$, ν, and μ are dropped for simplicity. The sign $\pm$ before each K is determined by the fermionic statistics of the carriers. The broadening energies $\gamma_{\mathbf{k}}$ in the denominators of the DR scattering amplitudes K are the sum of the broadenings of the corresponding electronic states (see Sec. II F). As examples, in $K^{\rm pd}_{ee1}\gamma^A_{\mathbf{k}} = \gamma^{\pi^*}_{\mathbf{k}} + \gamma^{\pi}_{\mathbf{k}}$, $\gamma^B_{\mathbf{k}} = \gamma^{\pi^*}_{\mathbf{k+q}} + \gamma^{\pi}_{\mathbf{k}}$, $\gamma^C_{\mathbf{k}} = \gamma^{\pi^*}_{\mathbf{k}} + \gamma^{\pi}_{\mathbf{k}}$. In $K^{\rm pd}_{eh1}\gamma^A_{\mathbf{k}} = \gamma^{\pi^*}_{\mathbf{k}} + \gamma^{\pi}_{\mathbf{k}}$, $\gamma^B_{\mathbf{k}} = \gamma^{\pi^*}_{\mathbf{k+q}} + \gamma^{\pi}_{\mathbf{k}}$, $\gamma^C_{\mathbf{k}} = \gamma^{\pi^*}_{\mathbf{k+q}} + \gamma^{\pi}_{\mathbf{k+q}}$.

There are eight phonon-defect (pd) processes. Process *ee*1:the electron is first scattered by a phonon and then by a defect,

$$K^{\rm pd}_{ee1} = \frac{\langle \mathbf{k}\pi | D_{\rm out} | \mathbf{k}\pi^* \rangle \langle \mathbf{k}\pi^* | H_D | \mathbf{k}+\mathbf{q},\pi^* \rangle \langle \mathbf{k}+\mathbf{q},\pi^* | \Delta H_{\mathbf{q},\nu} | \mathbf{k}\pi^* \rangle \langle \mathbf{k}\pi^* | D_{in} | \mathbf{k}\pi \rangle}{\left(\epsilon_L - \epsilon^{\pi^*}_{\mathbf{k}} + \epsilon^{\pi}_{\mathbf{k}} - \hbar\omega^{\nu}_{-\mathbf{q}} - i\frac{\gamma^C_{\mathbf{k}}}{2}\right)\left(\epsilon_L - \epsilon^{\pi^*}_{\mathbf{k+q}} + \epsilon^{\pi}_{\mathbf{k}} - \hbar\omega^{\nu}_{-\mathbf{q}} - i\frac{\gamma^B_{\mathbf{k}}}{2}\right)\left(\epsilon_L - \epsilon^{\pi^*}_{\mathbf{k}} + \epsilon^{\pi}_{\mathbf{k}} - i\frac{\gamma^A_{\mathbf{k}}}{2}\right)}.$$

Process *ee*2: the electron is first scattered by a defect and then by a phonon,

$$K^{\rm pd}_{ee2} = \frac{\langle \mathbf{k}\pi | D_{\rm out} | \mathbf{k}\pi^* \rangle \langle \mathbf{k}\pi^* | \Delta H_{\mathbf{q},\nu} | \mathbf{k}-\mathbf{q},\pi^* \rangle \langle \mathbf{k}-\mathbf{q},\pi^* | H_D | \mathbf{k}\pi^* \rangle \langle \mathbf{k}\pi^* | D_{in} | \mathbf{k}\pi \rangle}{\left(\epsilon_L - \epsilon^{\pi^*}_{\mathbf{k}} + \epsilon^{\pi}_{\mathbf{k}} - \hbar\omega^{\nu}_{-\mathbf{q}} - i\frac{\gamma^C_{\mathbf{k}}}{2}\right)\left(\epsilon_L - \epsilon^{\pi^*}_{\mathbf{k-q}} + \epsilon^{\pi}_{\mathbf{k}} - i\frac{\gamma^B_{\mathbf{k}}}{2}\right)\left(\epsilon_L - \epsilon^{\pi^*}_{\mathbf{k}} + \epsilon^{\pi}_{\mathbf{k}} - i\frac{\gamma^A_{\mathbf{k}}}{2}\right)}.$$

Process *hh*1: the hole is first scattered by a phonon and then by a defect,

$$K^{\rm pd}_{hh1} = \frac{\langle \mathbf{k}\pi | D_{\rm out} | \mathbf{k}\pi^* \rangle \langle \mathbf{k}-\mathbf{q},\pi | H_D | \mathbf{k}\pi \rangle \langle \mathbf{k}\pi | \Delta H_{\mathbf{q},\nu} | \mathbf{k}-\mathbf{q},\pi \rangle \langle \mathbf{k}\pi^* | D_{in} | \mathbf{k}\pi \rangle}{\left(\epsilon_L - \epsilon^{\pi^*}_{\mathbf{k}} + \epsilon^{\pi}_{\mathbf{k}} - \hbar\omega^{\nu}_{-\mathbf{q}} - i\frac{\gamma^C_{\mathbf{k}}}{2}\right)\left(\epsilon_L - \epsilon^{\pi^*}_{\mathbf{k}} + \epsilon^{\pi}_{\mathbf{k-q}} - \hbar\omega^{\nu}_{-\mathbf{q}} - i\frac{\gamma^B_{\mathbf{k}}}{2}\right)\left(\epsilon_L - \epsilon^{\pi^*}_{\mathbf{k}} + \epsilon^{\pi}_{\mathbf{k}} - i\frac{\gamma^A_{\mathbf{k}}}{2}\right)}.$$

Process $hh2$: the hole is first scattered by a defect and then by a phonon,

$$K^{\rm pd}_{hh2}=\frac{\langle \mathbf{k}\pi|D_{\rm out}|\mathbf{k}\pi^*\rangle\langle \mathbf{k}+\mathbf{q},\pi|\Delta H_{\mathbf{q},\nu}|\mathbf{k}\pi\rangle\langle \mathbf{k}\pi|H_D|\mathbf{k}+\mathbf{q},\pi\rangle\langle \mathbf{k}\pi^*|D_{in}|\mathbf{k}\pi\rangle}{\left(\epsilon_L-\epsilon^{\pi^*}_{\mathbf{k}}+\epsilon^{\pi}_{\mathbf{k}}-\hbar\omega^{\nu}_{-\mathbf{q}}-i\frac{\gamma^C_{\mathbf{k}}}{2}\right)\left(\epsilon_L-\epsilon^{\pi^*}_{\mathbf{k}}+\epsilon^{\pi}_{\mathbf{k}+\mathbf{q}}-i\frac{\gamma^B_{\mathbf{k}}}{2}\right)\left(\epsilon_L-\epsilon^{\pi^*}_{\mathbf{k}}+\epsilon^{\pi}_{\mathbf{k}}-i\frac{\gamma^A_{\mathbf{k}}}{2}\right)}.$$

Process $eh1$: first the electron is scattered by a phonon and then the hole by a defect,

$$K^{\rm pd}_{eh1}=-\frac{\langle \mathbf{k}+\mathbf{q},\pi|D_{\rm out}|\mathbf{k}+\mathbf{q},\pi^*\rangle\langle \mathbf{k}\pi|H_D|\mathbf{k}+\mathbf{q},\pi\rangle\langle \mathbf{k}+\mathbf{q},\pi^*|\Delta H_{\mathbf{q},\nu}|\mathbf{k}\pi^*\rangle\langle \mathbf{k}\pi^*|D_{in}|\mathbf{k}\pi\rangle}{\left(\epsilon_L-\epsilon^{\pi^*}_{\mathbf{k}+\mathbf{q}}+\epsilon^{\pi}_{\mathbf{k}+\mathbf{q}}-\hbar\omega^{\nu}_{-\mathbf{q}}-i\frac{\gamma^C_{\mathbf{k}}}{2}\right)\left(\epsilon_L-\epsilon^{\pi^*}_{\mathbf{k}+\mathbf{q}}+\epsilon^{\pi}_{\mathbf{k}}-\hbar\omega^{\nu}_{-\mathbf{q}}-i\frac{\gamma^B_{\mathbf{k}}}{2}\right)\left(\epsilon_L-\epsilon^{\pi^*}_{\mathbf{k}}+\epsilon^{\pi}_{\mathbf{k}}-i\frac{\gamma^A_{\mathbf{k}}}{2}\right)}.$$

Process $eh2$: first the electron is scattered by a defect and then the hole by a phonon,

$$K^{\rm pd}_{eh2}=-\frac{\langle \mathbf{k}-\mathbf{q},\pi|D_{\rm out}|\mathbf{k}-\mathbf{q},\pi^*\rangle\langle \mathbf{k}\pi|\Delta H_{\mathbf{q},\nu}|\mathbf{k}-\mathbf{q},\pi\rangle\langle \mathbf{k}-\mathbf{q},\pi^*|H_D|\mathbf{k}\pi^*\rangle\langle \mathbf{k}\pi^*|D_{in}|\mathbf{k}\pi\rangle}{\left(\epsilon_L-\epsilon^{\pi^*}_{\mathbf{k}-\mathbf{q}}+\epsilon^{\pi}_{\mathbf{k}-\mathbf{q}}-\hbar\omega^{\nu}_{-\mathbf{q}}-i\frac{\gamma^C_{\mathbf{k}}}{2}\right)\left(\epsilon_L-\epsilon^{\pi^*}_{\mathbf{k}-\mathbf{q}}+\epsilon^{\pi}_{\mathbf{k}}-i\frac{\gamma^B_{\mathbf{k}}}{2}\right)\left(\epsilon_L-\epsilon^{\pi^*}_{\mathbf{k}}+\epsilon^{\pi}_{\mathbf{k}}-i\frac{\gamma^A_{\mathbf{k}}}{2}\right)}.$$

Process $he1$: first the hole is scattered by a phonon and then the electron by a defect,

$$K^{\rm pd}_{he1}=-\frac{\langle \mathbf{k}-\mathbf{q},\pi|D_{\rm out}|\mathbf{k}-\mathbf{q},\pi^*\rangle\langle \mathbf{k}-\mathbf{q},\pi^*|H_D|\mathbf{k}\pi^*\rangle\langle \mathbf{k}\pi|\Delta H_{\mathbf{q},\nu}|\mathbf{k}-\mathbf{q},\pi\rangle\langle \mathbf{k}\pi^*|D_{in}|\mathbf{k}\pi\rangle}{\left(\epsilon_L-\epsilon^{\pi^*}_{\mathbf{k}-\mathbf{q}}+\epsilon^{\pi}_{\mathbf{k}-\mathbf{q}}-\hbar\omega^{\nu}_{-\mathbf{q}}-i\frac{\gamma^C_{\mathbf{k}}}{2}\right)\left(\epsilon_L-\epsilon^{\pi^*}_{\mathbf{k}}+\epsilon^{\pi}_{\mathbf{k}-\mathbf{q}}-\hbar\omega^{\nu}_{-\mathbf{q}}-i\frac{\gamma^B_{\mathbf{k}}}{2}\right)\left(\epsilon_L-\epsilon^{\pi^*}_{\mathbf{k}}+\epsilon^{\pi}_{\mathbf{k}}-i\frac{\gamma^Q_{\mathbf{k}}}{2}\right)}.$$

Process $he2$: first the hole is scattered by a defect and then the electron by a phonon,

$$K^{\rm pd}_{he2}=-\frac{\langle \mathbf{k}+\mathbf{q},\pi|D_{\rm out}|\mathbf{k}+\mathbf{q},\pi^*\rangle\langle \mathbf{k}+\mathbf{q},\pi^*|\Delta H_{\mathbf{q},\nu}|\mathbf{k}\pi^*\rangle\langle \mathbf{k}\pi|H_D|\mathbf{k}+\mathbf{q},\pi\rangle\langle \mathbf{k}\pi^*|D_{in}|\mathbf{k}\pi\rangle}{\left(\epsilon_L-\epsilon^{\pi^*}_{\mathbf{k}+\mathbf{q}}+\epsilon^{\pi}_{\mathbf{k}+\mathbf{q}}-\hbar\omega^{\nu}_{-\mathbf{q}}-i\frac{\gamma^C_{\mathbf{k}}}{2}\right)\left(\epsilon_L-\epsilon^{\pi^*}_{\mathbf{k}}+\epsilon^{\pi}_{\mathbf{k}+\mathbf{q}}-i\frac{\gamma^B_{\mathbf{k}}}{2}\right)\left(\epsilon_L-\epsilon^{\pi^*}_{\mathbf{k}}+\epsilon^{\pi}_{\mathbf{k}}-i\frac{\gamma^A_{\mathbf{k}}}{2}\right)}.$$

There are eight two-phonon (pp) processes. Process $ee1$: the electron is first scattered by the $-\mathbf{q}\nu$ phonon and then by the $\mathbf{q}\mu$ one,

$$K^{pp}_{ee1}=\frac{\langle \mathbf{k}\pi|D_{\rm out}|\mathbf{k}\pi^*\rangle\langle \mathbf{k}\pi^*|\Delta H_{-\mathbf{q},\mu}|\mathbf{k}+\mathbf{q},\pi^*\rangle\langle \mathbf{k}+\mathbf{q},\pi^*|\Delta H_{\mathbf{q},\nu}|\mathbf{k}\pi^*\rangle\langle \mathbf{k}\pi^*|D_{in}|\mathbf{k}\pi\rangle}{\left(\epsilon_L-\epsilon^{\pi^*}_{\mathbf{k}}+\epsilon^{\pi}_{\mathbf{k}}-\hbar\omega^{\nu}_{-\mathbf{q}}-\hbar\omega^{\mu}_{\mathbf{q}}-i\frac{\gamma^C_{\mathbf{k}}}{2}\right)\left(\epsilon_L-\epsilon^{\pi^*}_{\mathbf{k}+\mathbf{q}}+\epsilon^{\pi}_{\mathbf{k}}-\hbar\omega^{\nu}_{-\mathbf{q}}-i\frac{\gamma^B_{\mathbf{k}}}{2}\right)\left(\epsilon_L-\epsilon^{\pi^*}_{\mathbf{k}}+\epsilon^{\pi}_{\mathbf{k}}-i\frac{\gamma^A_{\mathbf{k}}}{2}\right)}.$$

Process $ee2$: the electron is first scattered by the $\mathbf{q}\mu$ phonon and then by the $-\mathbf{q}\nu$ one,

$$K^{pp}_{ee2}=\frac{\langle \mathbf{k}\pi|D_{\rm out}|\mathbf{k}\pi^*\rangle\langle \mathbf{k}\pi^*|\Delta H_{\mathbf{q},\nu}|\mathbf{k}-\mathbf{q},\pi^*\rangle\langle \mathbf{k}-\mathbf{q},\pi^*|\Delta H_{-\mathbf{q},\mu}|\mathbf{k}\pi^*\rangle\langle \mathbf{k}\pi^*|D_{in}|\mathbf{k}\pi\rangle}{\left(\epsilon_L-\epsilon^{\pi^*}_{\mathbf{k}}+\epsilon^{\pi}_{\mathbf{k}}-\hbar\omega^{\nu}_{-\mathbf{q}}-\hbar\omega^{\mu}_{\mathbf{q}}-i\frac{\gamma^C_{\mathbf{k}}}{2}\right)\left(\epsilon_L-\epsilon^{\pi^*}_{\mathbf{k}-\mathbf{q}}+\epsilon^{\pi}_{\mathbf{k}}-\hbar\omega^{\mu}_{\mathbf{q}}-i\frac{\gamma^B_{\mathbf{k}}}{2}\right)\left(\epsilon_L-\epsilon^{\pi^*}_{\mathbf{k}}+\epsilon^{\pi}_{\mathbf{k}}-i\frac{\gamma^A_{\mathbf{k}}}{2}\right)}.$$

Process $hh1$: the hole is first scattered by the $-\mathbf{q}\nu$ phonon and then by the $\mathbf{q}\mu$ one,

$$K^{pp}_{hh1}=\frac{\langle \mathbf{k}\pi|D_{\rm out}|\mathbf{k}\pi^*\rangle\langle \mathbf{k}-\mathbf{q},\pi|\Delta H_{-\mathbf{q},\mu}|\mathbf{k}\pi\rangle\langle \mathbf{k}\pi|\Delta H_{\mathbf{q},\nu}|\mathbf{k}-\mathbf{q},\pi\rangle\langle \mathbf{k}\pi^*|D_{in}|\mathbf{k}\pi\rangle}{\left(\epsilon_L-\epsilon^{\pi^*}_{\mathbf{k}}+\epsilon^{\pi}_{\mathbf{k}}-\hbar\omega^{\nu}_{-\mathbf{q}}-\hbar\omega^{\mu}_{\mathbf{q}}-i\frac{\gamma^C_{\mathbf{k}}}{2}\right)\left(\epsilon_L-\epsilon^{\pi^*}_{\mathbf{k}}+\epsilon^{\pi}_{\mathbf{k}-\mathbf{q}}-\hbar\omega^{\nu}_{-\mathbf{q}}-i\frac{\gamma^B_{\mathbf{k}}}{2}\right)\left(\epsilon_L-\epsilon^{\pi^*}_{\mathbf{k}}+\epsilon^{\pi}_{\mathbf{k}}-i\frac{\gamma^A_{\mathbf{k}}}{2}\right)}.$$

Process $hh2$: the hole is first scattered by the $\mathbf{q}\mu$ phonon and then by the $-\mathbf{q}\nu$ one,

$$K^{pp}_{hh2}=\frac{\langle \mathbf{k}\pi|D_{\rm out}|\mathbf{k}\pi^*\rangle\langle \mathbf{k}+\mathbf{q},\pi|\Delta H_{\mathbf{q},\nu}|\mathbf{k}\pi\rangle\langle \mathbf{k}\pi|\Delta H_{-\mathbf{q},\mu}|\mathbf{k}+\mathbf{q},\pi\rangle\langle \mathbf{k}\pi^*|D_{in}|\mathbf{k}\pi\rangle}{\left(\epsilon_L-\epsilon^{\pi^*}_{\mathbf{k}}+\epsilon^{\pi}_{\mathbf{k}}-\hbar\omega^{\nu}_{-\mathbf{q}}-\hbar\omega^{\mu}_{\mathbf{q}}-i\frac{\gamma^C_{\mathbf{k}}}{2}\right)\left(\epsilon_L-\epsilon^{\pi^*}_{\mathbf{k}}+\epsilon^{\pi}_{\mathbf{k}+\mathbf{q}}-\hbar\omega^{\mu}_{\mathbf{q}}-i\frac{\gamma^B_{\mathbf{k}}}{2}\right)\left(\epsilon_L-\epsilon^{\pi^*}_{\mathbf{k}}+\epsilon^{\pi}_{\mathbf{k}}-i\frac{\gamma^A_{\mathbf{k}}}{2}\right)}.$$

Process $eh1$: first the electron is scattered by the $-\mathbf{q}\nu$ phonon and then the hole by the $\mathbf{q}\mu$ one,

$$K^{pp}_{eh1}=-\frac{\langle \mathbf{k}+\mathbf{q},\pi|D_{\rm out}|\mathbf{k}+\mathbf{q},\pi^*\rangle\langle \mathbf{k}\pi|\Delta H_{-\mathbf{q},\mu}|\mathbf{k}+\mathbf{q},\pi\rangle\langle \mathbf{k}+\mathbf{q},\pi^*|\Delta H_{\mathbf{q},\nu}|\mathbf{k}\pi^*\rangle\langle \mathbf{k}\pi^*|D_{in}|\mathbf{k}\pi\rangle}{\left(\epsilon_L-\epsilon^{\pi^*}_{\mathbf{k}+\mathbf{q}}+\epsilon^{\pi}_{\mathbf{k}+\mathbf{q}}-\hbar\omega^{\nu}_{-\mathbf{q}}-\hbar\omega^{\mu}_{\mathbf{q}}-i\frac{\gamma^C_{\mathbf{k}}}{2}\right)\left(\epsilon_L-\epsilon^{\pi^*}_{\mathbf{k}+\mathbf{q}}+\epsilon^{\pi}_{\mathbf{k}}-\hbar\omega^{\nu}_{-\mathbf{q}}-i\frac{\gamma^B_{\mathbf{k}}}{2}\right)\left(\epsilon_L-\epsilon^{\pi^*}_{\mathbf{k}}+\epsilon^{\pi}_{\mathbf{k}}-i\frac{\gamma^A_{\mathbf{k}}}{2}\right)}.$$

Process $eh2$: first the electron is scattered by the $\mathbf{q}\mu$ phonon and then the hole by the $-\mathbf{q}\nu$ one,

$$K^{pp}_{eh2}=-\frac{\langle \mathbf{k}-\mathbf{q},\pi|D_{\rm out}|\mathbf{k}-\mathbf{q},\pi^*\rangle\langle \mathbf{k}\pi|\Delta H_{\mathbf{q},\nu}|\mathbf{k}-\mathbf{q},\pi\rangle\langle \mathbf{k}-\mathbf{q},\pi^*|\Delta H_{-\mathbf{q},\mu}|\mathbf{k}\pi^*\rangle\langle \mathbf{k}\pi^*|D_{in}|\mathbf{k}\pi\rangle}{\left(\epsilon_L-\epsilon^{\pi^*}_{\mathbf{k}-\mathbf{q}}+\epsilon^{\pi}_{\mathbf{k}-\mathbf{q}}-\hbar\omega^{\nu}_{-\mathbf{q}}-\hbar\omega^{\mu}_{\mathbf{q}}-i\frac{\gamma^C_{\mathbf{k}}}{2}\right)\left(\epsilon_L-\epsilon^{\pi^*}_{\mathbf{k}-\mathbf{q}}+\epsilon^{\pi}_{\mathbf{k}}-\hbar\omega^{\mu}_{\mathbf{q}}-i\frac{\gamma^B_{\mathbf{k}}}{2}\right)\left(\epsilon_L-\epsilon^{\pi^*}_{\mathbf{k}}+\epsilon^{\pi}_{\mathbf{k}}-i\frac{\gamma^A_{\mathbf{k}}}{2}\right)}.$$

Process $he1$: first the hole is scattered by the $-\mathbf{q}\nu$ phonon and then the electron by the $\mathbf{q}\mu$ one,

$$K^{pp}_{he1}=-\frac{\langle \mathbf{k}-\mathbf{q},\pi|D_{\rm out}|\mathbf{k}-\mathbf{q},\pi^*\rangle\langle \mathbf{k}-\mathbf{q},\pi^*|\Delta H_{-\mathbf{q},\mu}|\mathbf{k}\pi^*\rangle\langle \mathbf{k}\pi|\Delta H_{\mathbf{q},\nu}|\mathbf{k}-\mathbf{q},\pi\rangle\langle \mathbf{k}\pi^*|D_{in}|\mathbf{k}\pi\rangle}{\left(\epsilon_L-\epsilon^{\pi^*}_{\mathbf{k}-\mathbf{q}}+\epsilon^{\pi}_{\mathbf{k}-\mathbf{q}}-\hbar\omega^{\nu}_{-\mathbf{q}}-\hbar\omega^{\mu}_{\mathbf{q}}-i\frac{\gamma^C_{\mathbf{k}}}{2}\right)\left(\epsilon_L-\epsilon^{\pi^*}_{\mathbf{k}}+\epsilon^{\pi}_{\mathbf{k}-\mathbf{q}}-\hbar\omega^{\nu}_{-\mathbf{q}}-i\frac{\gamma^B_{\mathbf{k}}}{2}\right)\left(\epsilon_L-\epsilon^{\pi^*}_{\mathbf{k}}+\epsilon^{\pi}_{\mathbf{k}}-i\frac{\gamma^A_{\mathbf{k}}}{2}\right)}.$$

Process $he2$: first the hole is scattered by the $\mathbf{q}\mu$ phonon and then the electron by the $-\mathbf{q}\nu$ one,

$$K^{pp}_{he2}=-\frac{\langle \mathbf{k}+\mathbf{q},\pi|D_{\rm out}|\mathbf{k}+\mathbf{q},\pi^*\rangle\langle \mathbf{k}+\mathbf{q},\pi^*|\Delta H_{\mathbf{q},\nu}|\mathbf{k}\pi^*\rangle\langle \mathbf{k}\pi|\Delta H_{-\mathbf{q},\mu}|\mathbf{k}+\mathbf{q},\pi\rangle\langle \mathbf{k}\pi^*|D_{in}|\mathbf{k}\pi\rangle}{\left(\epsilon_L-\epsilon^{\pi^*}_{\mathbf{k}+\mathbf{q}}+\epsilon^{\pi}_{\mathbf{k}+\mathbf{q}}-\hbar\omega^{\nu}_{-\mathbf{q}}-\hbar\omega^{\mu}_{\mathbf{q}}-i\frac{\gamma^C_{\mathbf{k}}}{2}\right)\left(\epsilon_L-\epsilon^{\pi^*}_{\mathbf{k}}+\epsilon^{\pi}_{\mathbf{k}+\mathbf{q}}-\hbar\omega^{\mu}_{\mathbf{q}}-i\frac{\gamma^B_{\mathbf{k}}}{2}\right)\left(\epsilon_L-\epsilon^{\pi^*}_{\mathbf{k}}+\epsilon^{\pi}_{\mathbf{k}}-i\frac{\gamma^A_{\mathbf{k}}}{2}\right)}.$$

APPENDIX B: TIGHT-BINDING MODEL

Here we describe the tight-binding model, which is used to calculate the electronic structure, the electron-phonon, the electron-light, and the electron-defect scattering matrix elements.

1. Electronic structure

Let us call $|l,s\rangle$ the orthonormalized p_z orbital of the s atom (in graphene $s = 1,2$), in the position τ_s, in the cell identified by the lattice vectors $\mathbf{R}_l$ ($l = 1,\infty$). Let us consider the wave function (normalized in the unit cell)

$$|\mathbf{k},s\rangle = \sum_l e^{i\mathbf{k}\cdot(\mathbf{R}_l+\tau_s)}|l,s\rangle.$$

Given the tight-binding Hamiltonian H, $H_{\mathbf{k},s,s'} = \langle\mathbf{k},s|H|\mathbf{k},s'\rangle/N$ (N is the number of cells in the crystal) is the 2×2 matrix:

$$H_{\mathbf{k}} = \begin{pmatrix} g(\mathbf{k}) & f(\mathbf{k}) \\ f^*(\mathbf{k}) & g(\mathbf{k}) \end{pmatrix}, \tag{B1}$$

where

$$f(\mathbf{k}) = -t_1\sum_{i=1,3} e^{i\mathbf{k}\cdot\mathbf{C}_\mathbf{i}^1} - t_3\sum_{i=1,3} e^{i\mathbf{k}\cdot\mathbf{C}_\mathbf{i}^3} - t_4\sum_{i=1,6} e^{i\mathbf{k}\cdot\mathbf{C}_\mathbf{i}^4},$$
$$g(\mathbf{k}) = -t_2\sum_{i=1,6} e^{i\mathbf{k}\cdot\mathbf{C}_\mathbf{i}^2} - t_5\sum_{i=1,6} e^{i\mathbf{k}\cdot\mathbf{C}_\mathbf{i}^5} = g^*(\mathbf{k}). \tag{B2}$$

Here, t_i is the ith-neighbor hopping parameter. $\mathbf{C}_\mathbf{i}^\mathbf{1}$ are the three vectors connecting the $s = 1$ atom with its three nearest neighbors ($i = 1,3$). More in general, $\mathbf{C}_\mathbf{i}^\mathbf{j}$ are the vectors connecting the $s = 1$ atom with the ith atom in the jth neighborhood.

By diagonalizing $H_{\mathbf{k},s,s'}$,

$$\sum_{s'=1,2} H_{\mathbf{k},s,s'}a^\alpha_{\mathbf{k}s'} = \epsilon^\alpha_\mathbf{k} a^\alpha_{\mathbf{k}s},$$

one obtains the eigenvalues $\epsilon^\alpha_\mathbf{k}$ ($\alpha = \pi,\pi^*$) and the eigenwave functions $|\mathbf{k},\alpha\rangle = \sum_s a^\alpha_{\mathbf{k}s}|\mathbf{k},s\rangle$:

$$\epsilon^{\pi^*}_\mathbf{k} = g(\mathbf{k}) + |f(\mathbf{k})|, a^{\pi^*}_\mathbf{k} = \frac{1}{\sqrt{2}}\begin{pmatrix} 1 \\ \phi(\mathbf{k}) \end{pmatrix},$$
$$\epsilon^{\pi}_\mathbf{k} = g(\mathbf{k}) - |f(\mathbf{k})|, a^{\pi}_\mathbf{k} = \frac{1}{\sqrt{2}}\begin{pmatrix} 1 \\ -\phi(\mathbf{k}) \end{pmatrix}, \tag{B3}$$

where $\phi(\mathbf{k}) = f^*(\mathbf{k})/|f(\mathbf{k})|$.

Finally, here the overlap matrix is the identity because of the use of orthonormal p_z orbitals. An alternative, a precise description of the bands, can also be obtained by using a pristine (nonorthonormal) p_z orbital with only three neighbors' interaction parameters at the expense of using a nondiagonal overlap matrix (see, e.g., Refs. 49 and 50).

2. Electron-phonon scattering

Given a phonon mode $\mathbf{q}\nu$, with pulsation $\omega_{\mathbf{q}\nu}$ and polarization $\epsilon^{s,c}_{\mathbf{q},\nu}$ ($s = 1,2$ is an atomic index and $c = 1,3$ is a Cartersian coordinate index, $\epsilon^{s,c}_{\mathbf{q},\nu}$ is normalized to 1 in the unit cell, corresponding to a displacement $\epsilon^{s,c}_{\mathbf{q},\nu}e^{i\mathbf{q}\cdot(\mathbf{R}_l+\boldsymbol{\tau}_s)}$ of the s atom in the l unit cell), the electron-phonon scattering matrix element is

$$\langle\mathbf{k}+\mathbf{q},\alpha|\Delta H_{\mathbf{q},\nu}|\mathbf{k},\beta\rangle = \sqrt{\frac{\hbar}{2M\omega_{\mathbf{q},\nu}}}\sum_{s,c}\epsilon^{s,c}_{\mathbf{q},\nu} \times \left(a^\alpha_{\mathbf{k}+\mathbf{q}}\right)^\dagger \Delta H^{s,c}_{\mathbf{k}+\mathbf{q},\mathbf{k}} a^\beta_\mathbf{k}, \tag{B4}$$

where M is the carbon mass. All the unit cells give the same contribution and the bra-ket integration is done on the unit cell (with this choice the numerators of the scattering amplitudes are independent of the number of cells of the crystal). The 2×2 matrix $\Delta H^{s,c}_{\mathbf{k}+\mathbf{q},\mathbf{k}}$ is the derivative of the TB Hamiltonian with respect to a periodic displacement (with periodicity $\mathbf{q}$) of the atom s along the c Cartesian coordinate. By defining η_1 as the derivative of the nearest-neighbor hopping parameter t_1 with respect to the bond length,

$$\Delta H^{1,c}_{\mathbf{k}+\mathbf{q},\mathbf{k}} = \sqrt{3}\eta_1\begin{pmatrix} 0 & h_c(\mathbf{k}) \\ h^*_c(\mathbf{k}+\mathbf{q}) & 0 \end{pmatrix},$$
$$\Delta H^{2,c}_{\mathbf{k}+\mathbf{q},\mathbf{k}} = -\sqrt{3}\eta_1\begin{pmatrix} 0 & h_c(\mathbf{k}+\mathbf{q}) \\ h^*_c(\mathbf{k}) & 0 \end{pmatrix},$$
$$h_c(\mathbf{k}) = \sum_{i=1,3} e^{i\mathbf{k}\cdot\mathbf{C}_\mathbf{i}^1} C^1_{i,c}/a_0, \tag{B5}$$

where $C^1_{i,c}$ is the Cartesian component along the c direction of $\mathbf{C}_\mathbf{i}^\mathbf{1}$, and a_0 is the graphene lattice spacing.

3. Electron-light scattering

The electron-light interaction is calculated as

$$\langle\mathbf{k}\pi^*|D_{in}|\mathbf{k}\pi\rangle = \frac{e\vec{P}_{in}\cdot\left(a^\pi_\mathbf{k}\right)^\dagger\vec{\nabla}H(\mathbf{k})a^{\pi^*}_\mathbf{k}}{\epsilon_L},$$
$$\langle\mathbf{k}\pi|D_{\text{out}}|\mathbf{k}\pi^*\rangle = \frac{e\vec{P}_{\text{out}}\cdot\left(a^\pi_\mathbf{k}\right)^\dagger\vec{\nabla}H(\mathbf{k})a^{\pi^*}_\mathbf{k}}{\epsilon^{\text{out}}_L}, \tag{B6}$$

where $\vec{P}_{in}$ and $\vec{P}_{\text{out}}$ are the polarizations of the incident and scattered radiation, $\vec{\nabla}H(\mathbf{k})$ is the gradient of the TB Hamiltonian, and it is a 2×2 matrix. ϵ_L is the incident laser energy and ϵ^{out}_L is the scattered radiation energy [$\epsilon^{\text{out}}_L = \epsilon_L - \hbar\omega^\nu_{-\mathbf{q}}$ for a $K^{\text{pd}}(\mathbf{q},\nu)$ process and $\epsilon^{\text{out}}_L = \epsilon_L - \hbar\omega^\nu_{-\mathbf{q}} - \hbar\omega^\mu_\mathbf{q}$ for a $K^{pp}(\mathbf{q},\nu,\mu)$ process].

4. Electron-defect scattering

We consider three distinct kinds of defects. The electron-defect scattering operator is defined accordingly.

(i) The *on-site defect* changes the on-site TB parameter of the atom τ_1 by δV_0, in this case we will use the notation $H_D = V_{\text{on}}$ and

$$\langle\mathbf{k}\alpha|V_{\text{on}}|\mathbf{k}'\alpha\rangle = \frac{\delta V_0}{2}; \tag{B7}$$

$\alpha = \pi$ or π^*. Here we have considered τ_1 in the origin and here the bra-ket integration is done all over the space. (ii) The *hopping defect* changes the hopping parameter of two

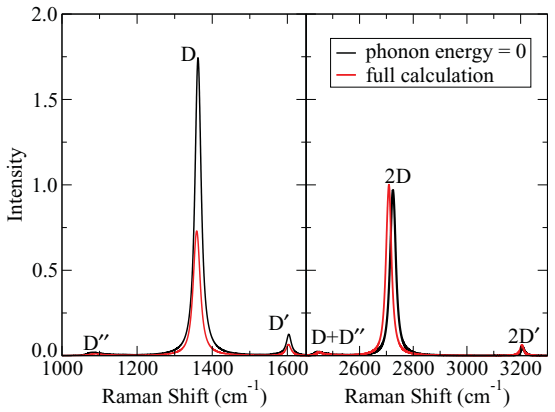

FIG. 27. (Color online) Comparison of a typical Raman spectrum (full calculation) with a test calculation in which the phonon energies in the denominators of the DR scattering amplitudes K are considered zero. Calculations are done using $\epsilon_L = 2.4$ eV, $\gamma^{\rm tot} = 96$ meV, and hopping defects with $\alpha_{\rm hopp} = 6.4 \times 10^{13}$ eV^2 cm^{-2}. All the intensities are normalized to the $2D$ line maximum value of the full calculation.

nearest-neighbor atoms connected by the vector C_i^1 by δt_1. $H_D = V_{\rm hopp}$ and

$$\langle \mathbf{k}\alpha | V_{\rm hopp} | \mathbf{k}'\alpha \rangle = \frac{\delta t_1}{2}\left[\phi^*(\mathbf{k}) e^{-i\mathbf{k}\cdot\mathbf{C_i^1}} + \phi(\mathbf{k}') e^{i\mathbf{k}'\cdot\mathbf{C_i^1}}\right], \quad \text{(B8)}$$

where ϕ is defined as in Eq. (B3). In the calculations of the Raman scattering probability averages among the three different C_i^1 vectors are taken.

(iii) The *Coulomb defect* is a Coulomb impurity with charge e, placed at a distance h from the graphene sheet. In this case, $H_D = V_{\rm Coul}$. The Coulomb potential in the position $\mathbf{r}$ in the graphene's plane is

$$V_{\rm Coul}(\mathbf{r}) = \frac{e^2}{4\pi\epsilon_0\kappa}\frac{1}{\sqrt{r^2+h^2}} = \frac{e^2}{4\pi\epsilon_0\kappa}\int d^2k \frac{e^{-{\rm kh}}}{k} e^{i\mathbf{k}\cdot\mathbf{r}}, \quad \text{(B9)}$$

where ϵ_0 is the vacuum permittivity, κ is an environment dielectric constant, and the integral is performed on all the reciprocal space. By assuming that the p_z orbitals are localized with respect to a_0 and h (this is done to avoid the introduction of new parameters in the model),

$$\langle \mathbf{k}\alpha | V_{\rm Coul} | \mathbf{k}'\alpha \rangle = \frac{e^2}{2\epsilon_0\kappa A_0}\sum_{\mathbf{G}} \frac{e^{-|\mathbf{k}-\mathbf{k}'+\mathbf{G}|h}}{|\mathbf{k}-\mathbf{k}'+\mathbf{G}|} \times [1 + e^{i(\mathbf{k}-\mathbf{k}'+\mathbf{G})\cdot\mathbf{C_1^1}}\phi^*(\mathbf{k})\phi(\mathbf{k}')], \quad \text{(B10)}$$

where the sum is done on the reciprocal-lattice vectors $\mathbf{G}$ and A_0 is the unit-cell area.

Note that in the three cases the Raman intensity is calculated by Eqs. (2) and (3). As a consequence, for the cases of on-site and hopping defects the intensity is proportional to $\alpha_{\rm on} = n_d \delta V_0^2$ and $\alpha_{\rm hopp} = n_d \delta t_1^2$, respectively, being n_d the impurity concentration. On the other hand, for the Coulomb impurities, the intensity is proportional to n_d, but it also depends on the impurity-graphene distance h, as in Eq. (B10) above.

APPENDIX C: ROLE OF THE PHONON ENERGIES IN THE DR

The Raman spectra depend on the phonon frequencies $\omega_{\mathbf{q}}^{\nu}$ through the energy conservation between the initial and the final states [expressed in the δ functions in Eq. (2)] and through the denominators of the DR scattering amplitudes K [e.g., in Eqs. (4) and (5)]. We performed a series of test calculations in which we consider the phonon energies $\omega_{\mathbf{q}}^{\nu} = 0$ in all the denominators of the amplitudes K [e.g., $\omega_{-\mathbf{q}}^{\nu} = \omega_{\mathbf{q}}^{\mu} = 0$ in Eqs. (4) and (5)]. It turns out that, qualitatively, the Raman spectra are not affected. For example, the $2D$ line intensity is basically unchanged, while the D one remains of the same orders of magnitude (Fig. 27). We also checked that the results of Sec. III E 1 are not affected by the actual value of $\omega_{\mathbf{q}}^{\nu}$ in the denominators. Using the notation of Sec. III E 1, by letting $\omega_{\mathbf{q}}^{\nu} = 0$ in the K denominators, $I_{ab} \gg I_{aa}$ and $\tilde{I}_{aa} \sim \tilde{I}_{ab}$ for both the $2D$ and the D lines. That is, the ab processes are still, by far, the dominant ones.

APPENDIX D: A SIMPLE MODEL

In Sec. III E 1 we have shown that the largest part of the DR Raman spectrum is due to the processes involving the scattering of both one electron and one hole (ab processes). We now show that the same conclusions are reached by considering a simple model in which the scattering matrix elements in the numerator of Eq. (1) are constant, the phonon energies in the denominators [e.g., $\hbar\omega_{\mathbf{q}}^{\nu}$ in Eqs. (4) and (5)] are neglected (see discussion in Appendix C), and in which the electronic bands are conic: $\epsilon_{\mathbf{k}}^{\pi^*/\pi} = \pm\hbar v_F |\mathbf{k}|$, where v_F is the Fermi velocity and $\mathbf{k=0}$ corresponds to the high symmetry $\mathbf{K}$ point.

For a given excitation energy ϵ_L, the scattering cross sections associated to a phonon of momentum $\mathbf{q}$ are $I_{aa}(\mathbf{q},\epsilon_L)$ and $I_{ab}(\mathbf{q},\epsilon_L)$. As usual, aa refers to the $ee1$, $ee2$, $hh1$, and $hh2$ processes, and ab to the $eh1$, $eh2$, $he1$, and $he2$ ones. By using the equations of Appendix A, one obtains

$$I_{aa}(\mathbf{q},\epsilon_L) = \left|\int \frac{d^2\mathbf{k}}{(2\pi)^2} K_{aa}(\mathbf{k},\mathbf{q},\epsilon_L)\right|^2, \quad I_{ab}(\mathbf{q},\epsilon_L) = \left|\int \frac{d^2\mathbf{k}}{(2\pi)^2} K_{ab}(\mathbf{k},\mathbf{q},\epsilon_L)\right|^2,$$
$$K_{aa}(\mathbf{k},\mathbf{q},\epsilon_L) = \frac{1}{\left(\epsilon_L - 2\hbar v_F k - i\frac{\gamma}{2}\right)\left(\epsilon_L - \hbar v_F|\mathbf{k}+\mathbf{q}| - \hbar v_F k - i\frac{\gamma}{2}\right)\left(\epsilon_L - 2\hbar v_F k - i\frac{\gamma}{2}\right)}, \quad \text{(D1)}$$
$$K_{ab}(\mathbf{k},\mathbf{q},\epsilon_L) = \frac{1}{\left(\epsilon_L - 2\hbar v_F|\mathbf{k}+\mathbf{q}| - i\frac{\gamma}{2}\right)\left(\epsilon_L - \hbar v_F|\mathbf{k}+\mathbf{q}| - \hbar v_F k - i\frac{\gamma}{2}\right)\left(\epsilon_L - 2\hbar v_F k - i\frac{\gamma}{2}\right)}.$$

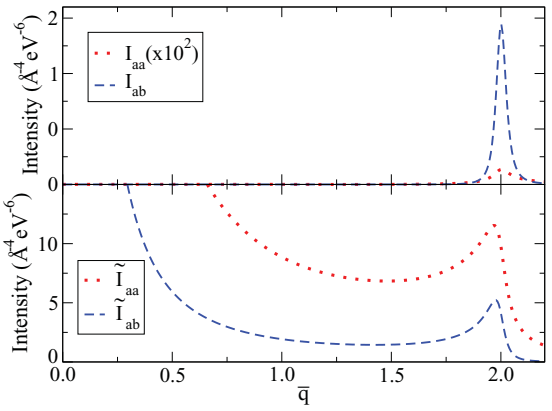

FIG. 28. (Color online) Numerical solution of Eqs. (D1) using $\epsilon_L = 2.4$ eV, $\gamma = 84$ meV, and $\hbar v_F = 6.49$ eV Å. $\overline{q} = 2q\hbar v_F/\epsilon_L$ is an adimensional momentum and $\overline{q} = 2$ corresponds to the double-resonance condition. I_{aa} is magnified by 10^2 for clarity. $\tilde{I}_{aa}$ and $\tilde{I}_{ab}$ are intensities in which quantum interference has been artificially suppressed (see the text).

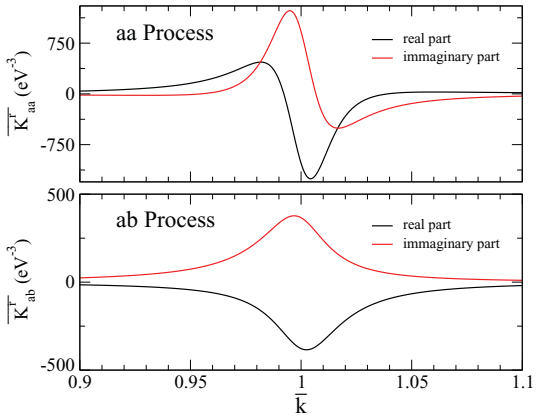

FIG. 29. (Color online) DR scattering amplitudes $\overline{K^r}$ as defined in Eq. (D2) for the aa and ab processes, as a function of the adimensional momentum $\overline{k} = 2k\hbar v_F/\epsilon_L$. The real and imaginary part of the complex number $\overline{K^r}$ are plotted as two different lines. Calculations are done using $\epsilon_L = 2.4$ eV, $\gamma = 84$ meV, and $\hbar v_F = 6.49$ eV Å.

In analogy to Sec. III E 1, $\tilde{I}_{aa}$ and $\tilde{I}_{ab}$ are obtained by considering only the modulus of the integrand, e.g., $\tilde{I}_{aa} = |\int d^2\mathbf{k}/(2\pi)^2|K_{aa}||^2$. Figure 28 reports the intensities I thus obtained for a fixed value of ϵ_L, as a function of q (the results do not depend on the direction of $\mathbf{q}$). As expected from the DR picture, $I(q)$ has a maximum at $q = \epsilon_L/(\hbar v_F)$. Even with this simplified model, one recovers the result that ab processes are by far dominant: $I_{ab} \gg I_{aa}$ from Fig. 28. The importance of quantum interference effects is understood by considering that the intensities $\tilde{I}_{ab}$ and $\tilde{I}_{aa}$ (in which quantum interference effects are artificially canceled; Sec. III E 1) are very different from I_{ab} and I_{aa}. In particular, $\tilde{I}_{ab}$ and $\tilde{I}_{aa}$ have the same order of magnitude. As already noticed in Ref. 29 the shapes of $I(q)$ and $\tilde{I}(q)$ are very different, thus the fact that $I(q)$ is associated to a well defined narrow line is a direct consequence of quantum interference. Notice that, however, the authors of Ref. 29 consider only the aa processes.

To further explain the concept of quantum interference we consider that for a fixed value of ϵ_L the resonance condition $q_r = \epsilon_L/(\hbar v_F)$ ($\overline{q} = 2$ in Fig. 28) implies that the maximum of the intensities are

$$I_\alpha(q_r, \epsilon_L) = \left| \int_0^\infty \frac{kdk}{2\pi} \overline{K^r_\alpha}(k) \right|^2, \tag{D2}$$

where the label $\alpha = aa$ or ab, and $\overline{K^r_\alpha}(k)$ are the K scattering amplitudes of Eqs. (D1) calculated at ϵ_L and q_r, averaged over the angular dependence of $\mathbf{k}$.

Figure 29 shows $\overline{K^r_{aa}}(k)$ and $\overline{K^r_{ab}}(k)$ for realistic values of the parameters ϵ_L, γ, and v_F. Both $\overline{K^r_{aa}}(k)$ and $\overline{K^r_{ab}}(k)$ have a maximum near $k = \epsilon_L/(2\hbar v_F)$, which corresponds to the DR condition ($\overline{k} = 1$ in Fig. 29). First we remark that, for realistic values of γ, the real, Re, and imaginary parts, Im, of the $\overline{K^r}$ amplitudes are of the same order of magnitude. Thus the $\overline{K^r}$ cannot be approximated as purely real or purely imaginary numbers. Second we notice that Re($\overline{K^r_{ab}}$) and Im($\overline{K^r_{ab}}$) do not change their sign when plotted as a function of k. On the contrary, Re($\overline{K^r_{aa}}$) and Im($\overline{K^r_{aa}}$) change their sign (Fig. 29). Because of this, the $\overline{K^r_{ab}}(k)$ inside the integral of Eq. (D2) add coherently, while the $\overline{K^r_{aa}}(k)$ interfere in a destructive way. As a consequence, $I_{ab} \gg I_{aa}$, despite the fact that $\overline{K^r_{ab}}$ and $\overline{K^r_{aa}}$ are of the same order of magnitude.

[1] A. C. Ferrari, J. C. Meyer, V. Scardaci, C. Casiraghi, M. Lazzeri, F. Mauri, S. Piscanec, D. Jiang, K. S. Novoselov, S. Roth, and A. K. Geim, Phys. Rev. Lett. **97**, 187401 (2006).

[2] A. Gupta, G. Chen, P. Joshi, S. Tadigadapa, and P. C. Eklund, Nano Lett. **6**, 2667 (2006).

[3] M. Lazzeri and F. Mauri, Phys. Rev. Lett. **97**, 266407 (2006).

[4] S. Pisana, M. Lazzeri, C. Casiraghi, K. S. Novoselov, A. K. Geim, A. C. Ferrari, and F. Mauri, Nat. Mater. **6**, 198 (2007).

[5] J. Yan, Y. Zhang, P. Kim, and A. Pinczuk, Phys. Rev. Lett. **98**, 166802 (2007).

[6] J. H. Chen, W. G. Cullen, C. Jang, M. S. Fuhrer, and E. D. Williams, Phys. Rev. Lett. **102**, 236805 (2009).

[7] M. M. Lucchese, F. Stavale, E. H. Martins Ferreira, C. Vilani, M. V. O. Moutinho, R. B. Capaz, C. A. Achete, and A. Jorio, Carbon **48**, 1592 (2010).

[8] Z. H. Ni, L. A. Ponomarenko, R. R. Nair, R. Yang, S. Anissimova, I. V. Grigorieva, F. Schedin, Z. X. Shen, E. H. Hill, K. S. Novoselov, and A. K. Geim, Nano Lett. **10**, 3868 (2010).

[9] D. L. Mafra, G. Samsonidze, L. M. Malard, D. C. Elias, J. C. Brant, F. Plentz, E. S. Alves, and M. A. Pimenta, Phys. Rev. B **76**, 233407 (2007). In this work, the $2D$ and $D + D''$ bands were called G' and $G*$, respectively.

[10] C. Thomsen and S. Reich, Phys. Rev. Lett. **85**, 5214 (2000).

[11]E. H. Martins Ferreira, M. V. O. Moutinho, F. Stavale, M. M. Lucchese, R. B. Capaz, C. A. Achete, and A. Jorio, Phys. Rev. B **82**, 125429 (2010).
[12]S. Berciaud, S. Ryu, L. E. Brus, and T. F. Heinz, Nano Lett. **9**, 346 (2009).
[13]R. M. Martin and L. M. Falicov, in *Light Scattering in Solids I*, Topics in Applied Physics Vol. 8, edited by M. Cardona (Springer, Berlin, 1983), p. 79.
[14]J. Kurti, V. Zolyomi, A. Gruneis, and H. Kuzmany, Phys. Rev. B **65**, 165433 (2002).
[15]R. Narula and S. Reich, Phys. Rev. B **78**, 165422 (2008).
[16]D. M. Basko, Phys. Rev. B **78**, 125418 (2008).
[17]J. S. Park, A. Reina, R. Saito, J. Kong, G. Dresselhaus, and M. S. Dresselhaus, Carbon **47**, 1303 (2009).
[18]D. L. Mafra, E. A. Moujaes, S. K. Doorn, H. Htoon, R. W. Nunes, and M. A. Pimenta, Carbon **49**, 1511 (2011).
[19]M. Mohr, J. Maultzsch, and C. Thomsen, Phys. Rev. B **82**, 201409(R) (2010).
[20]M. Huang, H. Yan, T. F. Heinz, and J. Hone, Nano Lett. **10**, 4074 (2010).
[21]O. Frank, M. Mohr, J. Maultzsch, C. Thomsen, I. Riaz, R. Jalil, K. S. Novoselov, G. Tsoukleri, J. Parthenios, K. Papagelis, L. Kavan, and C. Galiotis, ACS Nano **5**, 2231 (2011).
[22]D. Yoon, Y. W. Son, and H. Cheong, Phys. Rev. Lett. **106**, 155502 (2011).
[23]D. M. Basko, Phys. Rev. B **76**, 081405(R) (2007).
[24]P. Gava, M. Lazzeri, A. M. Saitta, and F. Mauri, Phys. Rev. B **79**, 165431 (2009).
[25]A. Gruneis, C. Attaccalite, L. Wirtz, H. Shiozawa, R. Saito, T. Pichler, and A. Rubio, Phys. Rev. B **78**, 205425 (2008).
[26]S. Baroni, S. de Gironcoli, A. Dal Corso, and P. Giannozzi, Rev. Mod. Phys. **73**, 515 (2001).
[27]M. Lazzeri, C. Attaccalite, L. Wirtz, and F. Mauri, Phys. Rev. B **78**, 081406 (2008).
[28]A. Grüneis, J. Serrano, A. Bosak, M. Lazzeri, S. L. Molodtsov, L. Wirtz, C. Attaccalite, M. Krisch, A. Rubio, F. Mauri, and T. Pichler, Phys. Rev. B **80**, 085423 (2009).
[29]J. Maultzsch, S. Reich, and C. Thomsen, Phys. Rev. B **70**, 155403 (2004).
[30]J. Maultzsch, S. Reich, C. Thomsen, H. Requardt, and P. Ordejon, Phys. Rev. Lett. **92**, 075501 (2004).
[31]M. Mohr, J. Maultzsch, E. Dobardzic, S. Reich, I. Milosevic, M. Damnjanovic, A. Bosak, M. Krisch, and C. Thomsen, Phys. Rev. B **76**, 035439 (2007).
[32]S. Piscanec, M. Lazzeri, F. Mauri, A. C. Ferrari, and J. Robertson, Phys. Rev. Lett. **93**, 185503 (2004).
[33]E. H. Hwang and S. Das Sarma, Phys. Rev. B **77**, 195412 (2008).
[34]D. M. Basko, S. Piscanec, and A. C. Ferrari, Phys. Rev. B **80**, 165413 (2009).
[35]I. Calizo, I. Bejenari, M. Rahman, G. Liu, and A. A. Balandin, J. Appl. Phys. **106**, 043509 (2009).
[36]C. Cong, T. Yu, R. Saito, G. F. Dresselhaus, and M. S. Dresselhaus, ACS Nano **5**, 1600 (2011).
[37]R. Rao, R. Podila, R. Tsuchikawa, J. Katoch, D. Tishler, A. M. Rao, and M. Ishigami, ACS Nano **5**, 1594 (2011).
[38]S. Reich and C. Thomsen, Philos. Trans. R. Soc. London, Ser. A **362**, 2271 (2010).
[39]D. Yoon, H. Moon, Y. W. Son, G. Samsonidze, B. H. Park, J. B. Kim, Y. P. Lee, and H. Cheong, Nano Lett. **8**, 4270 (2008).
[40]C. Attaccalite, L. Wirtz, M. Lazzeri, F. Mauri, and A. Rubio, Nano Lett. **10**, 1172 (2010).
[41]F. Alzina, H. Tao, J. Moser, Y. Garcia, A. Bachtold, and C. M. Sotomayor-Torres, Phys. Rev. B **82**, 075422 (2010).
[42]A. C. Ferrari and J. Robertson, Phys. Rev. B **61**, 14095 (2000).
[43]J. H. Chen, C. Jang, S. Adam, M. S. Fuhrer, E. D. Williams, and M. Ishigami, Nat. Phys. **4**, 377 (2008).
[44]D. M. Basko, Phys. Rev. B **79**, 205428 (2009).
[45]Reference 44 predicts (last sentence of Sec. II B) that for the D line, the aa processes should be weaker by a factor $\hbar\omega_{ph}/\epsilon_L$, where ω_{ph} is the **K** phonon pulsation. We verified by direct calculations that this relation does not apply to the present results. Indeed, by considering $\omega_{ph} = 0$ in the denominators of the Raman scattering matrix elements K [e.g., in Eqs. (4) and (5)] the ratio I_{aa}/I_{ab} increases by 25% instead of decreasing to zero as predicted by Ref. 44.
[46]In Fig. 20, the mapping of the Raman intensity in the first BZ is done by integrating in the following frequency windows: [1040 cm^{-1}, 1180 cm^{-1}] for the D'' line; [1200 cm^{-1}, 1520 cm^{-1}] for D; [1520 cm^{-1}, 1720 cm^{-1}] for D'; [2380 cm^{-1}, 2550 cm^{-1}] for $D + D''$; [2550 cm^{-1}, 3000 cm^{-1}] for $2D$; [3120 cm^{-1}, 3300 cm^{-1}] for $2D'$. In Fig. 26, the mapping is done by integrating in the windows: [2760 cm^{-1}, 2793 cm^{-1}] for $2D^-$; [2793 cm^{-1}, 3060 cm^{-1}] for $2D^+$.
[47]R. Saito, A. Jorio, A. G. Souza Filho, G. Dresselhaus, M. S. Dresselhaus, and M. A. Pimenta, Phys. Rev. Lett. **88**, 027401 (2001).
[48]L. G. Cançado, M. A. Pimenta, R. Saito, A. Jorio, L. O. Ladeira, A. Grueneis, A. G. Souza-Filho, and G. Dresselhaus, and M. S. Dresselhaus, Phys. Rev. B **66**, 035415 (2002).
[49]S. Reich, J. Maultzsch, and C. Thomsen, and P. Ordejon, Phys. Rev. B **66**, 035412 (2002).
[50]A. Grüneis, C. Attaccalite, L. Wirtz, H. Shiozawa, R. Saito, T. Pichler, and A. Rubio, Phys. Rev. B **78**, 205425 (2008).